

Tesseral 2.5D-3C Modeling

Outline

Basic theory and validation tests for different models

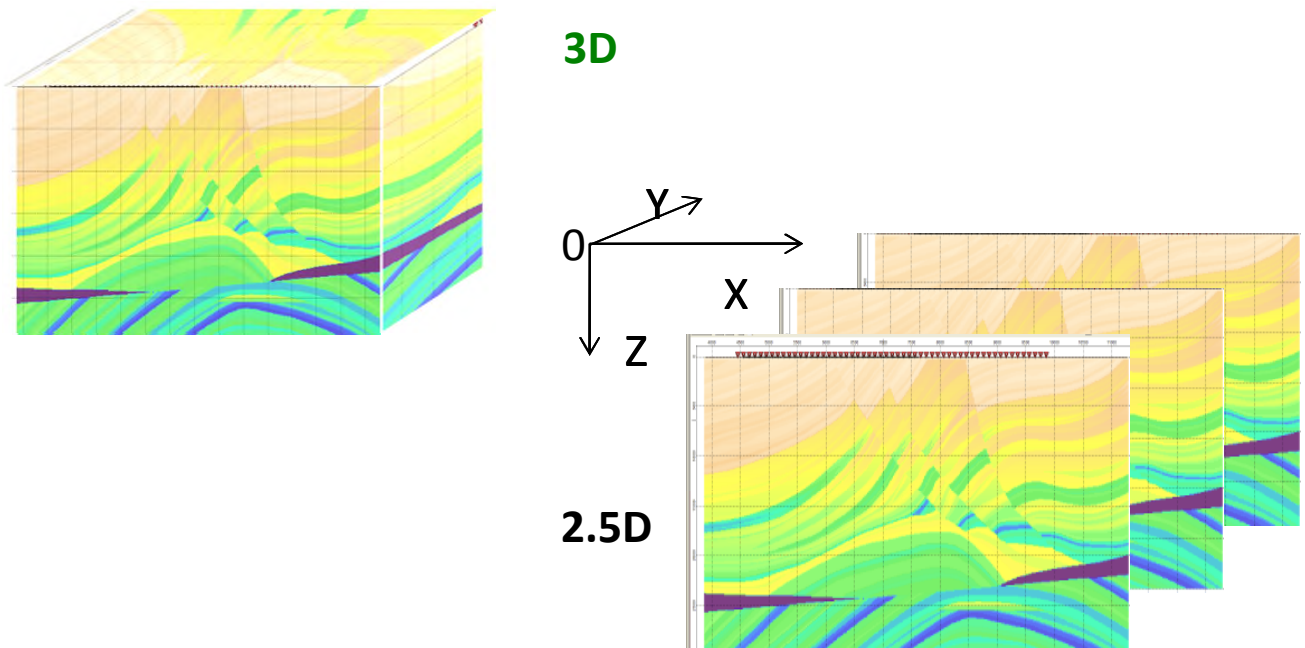
- ❖ Basic theory of 2.5D-3C modeling
 - ❑ 2-Layer model with the lower HTI layer
 - ❑ 2-layer model with both HTI layers
 - ❑ Multi-layered isotropic-HTI model
 - ❑ Model with thin-interbedded layer and AVO
 - ❑ Azimuthal AVO and AVOT
 - ❑ 2.5D Marmousi model
 - ❑ Model with 3 vertical boundaries
- ❖ 2.5D-9C modeling
- ❖ Modeling of Lamb- Stoneley tube waves



www.tesseral-geo.com

❖ Basic theory of 2.5D-3C modeling

- ❖ 2.5D modeling assumes the model parameters to be constant along the OY-axis (Figure below). However, the symmetry axis of the anisotropy parameters can be oriented in arbitrary spatial direction.
- ❖ Unlike 2D modeling, 2.5D modeling can simulate wave propagation in three dimensions. For the case of TTI anisotropy, 2.5D modeling can simulate both “fast” and “slow” shear waves and takes into account all of their properties such as double refraction.



Example of 2.5D model. Model parameters are constant along OY-axis

Different from the 3D model, the 2.5D model parameters, including the velocities of P- and S-waves, densities, parameters of anisotropy and fractured systems, is constant along one of axis, usually along Y axis. But the inclination and the azimuth of the anisotropy symmetry axis and the fracture systems may be oriented in space arbitrarily.

As contrary to 2D case, the wave is propagating in the 3D space in full accordance with the 3D wave equation. It accounts for the effect of geometrical divergence correctly, and there is no signal distortion during the wave propagation. For the S waves, all the propagation laws are complied, for example, the birefringence with presence of the fast and slow S waves within fractured media

◆ Basic theory of 2.5D-3C modeling

3D-3C wave-propagation equations in arbitrary medium

$$\rho(\vec{x}) \frac{\partial u_i(\vec{x}, t)}{\partial t} = \frac{\partial \tau_{ij}(\vec{x}, t)}{\partial x_j} + f_i(\vec{x}, t)$$

$\mathbf{u} = (u_1, u_2, u_3)$ is the velocity vector.

$\boldsymbol{\tau} = (\tau_{11}, \tau_{22}, \tau_{33}, \tau_{23}, \tau_{13}, \tau_{12})$ is the vector of stress tensor components.

$$\frac{\partial \tau_{ij}}{\partial t} = \lambda_{ijpq}(\vec{x}) \frac{\partial u_p(\vec{x}, t)}{\partial x_q} + \frac{\partial M_{ij}(\vec{x}, t)}{\partial t}$$

λ_{ijpq} is elastic moduli.

f_i is the applied force within the body volume.

M_{ij} is the tensor of moment.

The wave equation is shown for the 3D case, where \mathbf{U} is the vector of displacement velocity of the medium particles, and $\boldsymbol{\tau}$ is the vector component of the stress tensor. In this set of equations, the upper one is the Newton's law governing the kinematics, and the lower one is the Hooke's law governing the relationship between strain and stress.

Displacement equations after Fourier-transform along variable x_2

$$\frac{\partial}{\partial t} \begin{pmatrix} u_1 \\ u_2 \\ u_3 \end{pmatrix} = \frac{1}{\rho} \begin{pmatrix} \tau_{11} & \tau_{12} & \tau_{13} \\ \tau_{12} & \tau_{22} & \tau_{23} \\ \tau_{13} & \tau_{23} & \tau_{33} \end{pmatrix} \begin{pmatrix} \frac{\partial}{\partial x_1} \\ ik_2 \\ \frac{\partial}{\partial x_3} \end{pmatrix}$$

$$\varepsilon_{11} = \frac{\partial u_1}{\partial x_1}$$

$$\varepsilon_{12} = ik_2 u_1 + \frac{\partial u_2}{\partial x_1}$$

$$\varepsilon_{13} = \frac{\partial u_1}{\partial x_3} + \frac{\partial u_3}{\partial x_1}$$

$$\varepsilon_{22} = ik_2 u_2$$

$$\varepsilon_{23} = \frac{\partial u_2}{\partial x_3} + ik_2 u_3$$

$$\varepsilon_{33} = \frac{\partial u_3}{\partial x_3}$$

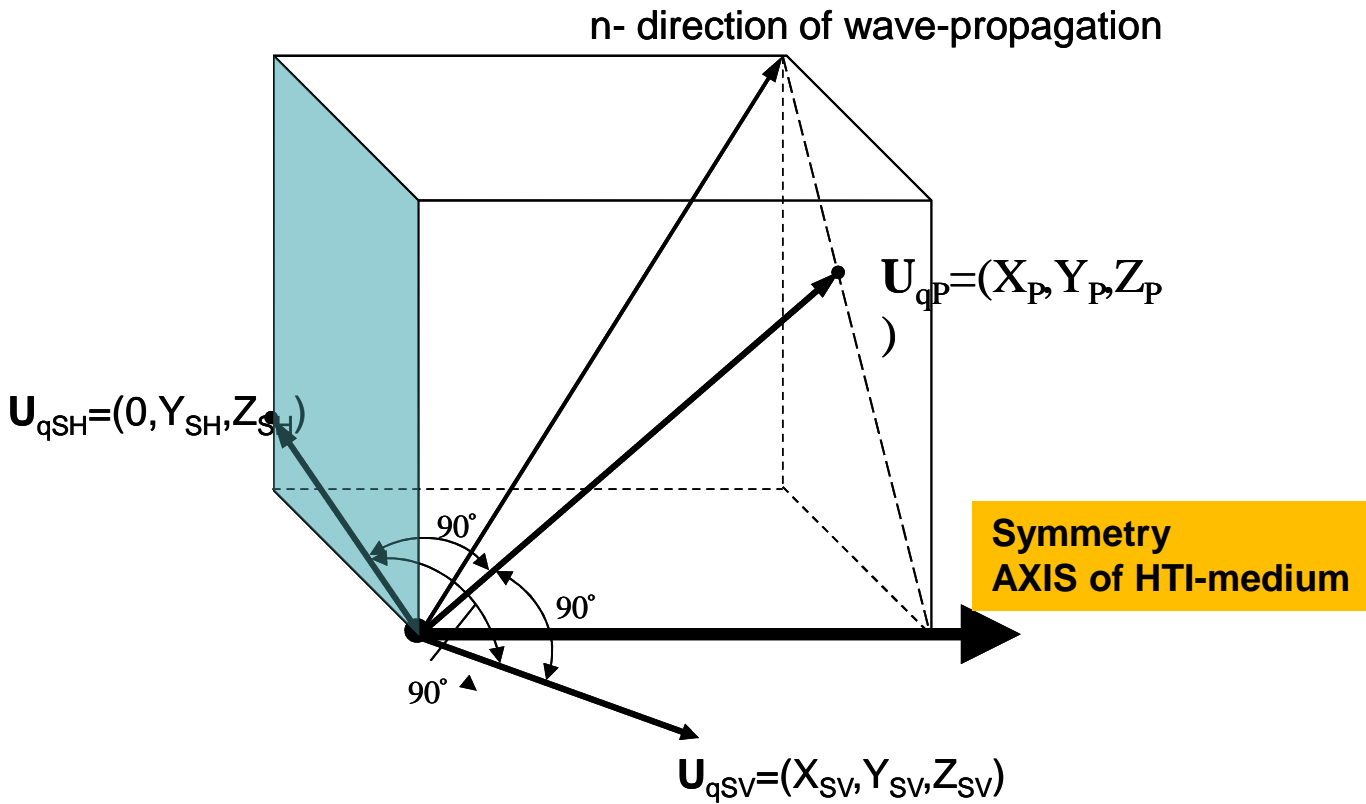
$$\frac{\partial}{\partial t} \begin{pmatrix} \tau_{11} \\ \tau_{23} \\ \tau_{33} \\ \tau_{23} \\ \tau_{13} \\ \tau_{12} \end{pmatrix} = \begin{pmatrix} a_{11} & a_{12} & a_{13} & a_{14} & a_{15} & a_{16} \\ a_{12} & a_{22} & a_{32} & a_{42} & a_{52} & a_{62} \\ a_{13} & a_{23} & a_{33} & a_{43} & a_{53} & a_{63} \\ a_{14} & a_{24} & a_{34} & a_{44} & a_{54} & a_{64} \\ a_{15} & a_{25} & a_{35} & a_{45} & a_{55} & a_{65} \\ a_{16} & a_{26} & a_{36} & a_{46} & a_{56} & a_{66} \end{pmatrix} \begin{pmatrix} \varepsilon_{11} \\ \varepsilon_{22} \\ \varepsilon_{33} \\ \varepsilon_{23} \\ \varepsilon_{13} \\ \varepsilon_{12} \end{pmatrix}$$

$$\mathbf{u}(x_1, x_2, x_3, t) = \sum_{K_2} \exp(ik_2 x_2) \mathbf{u}(x_1, k_2, x_3, t)$$

The mathematical basis of 2.5D modeling is shown. After applying the Fourier transform along the X_2 or Y axis, this set of equations reduce to the form as shown in the **Slide 5**. K_2 is the spatial frequency along the axis Y , \mathbf{A} is the elasticity matrix, $\boldsymbol{\varepsilon}$ is strain vector. For each K_2 of harmonics, the set of equations is split into the pseudo-2D wave equations, which may be solved independently by individual processor of the cluster. By such way, the good load-balance parallelization of the simulation phase (not the merging phase) is done without inter-processor interaction, and this fact gives an essential advantage of parallel implementation, as compared to the 3D modeling.

After the simulation phase, the partial solutions for each spatial frequency are transformed into spatial gathers, by using inverse Fourier transform.

❖ Basic theory of 2.5D modeling



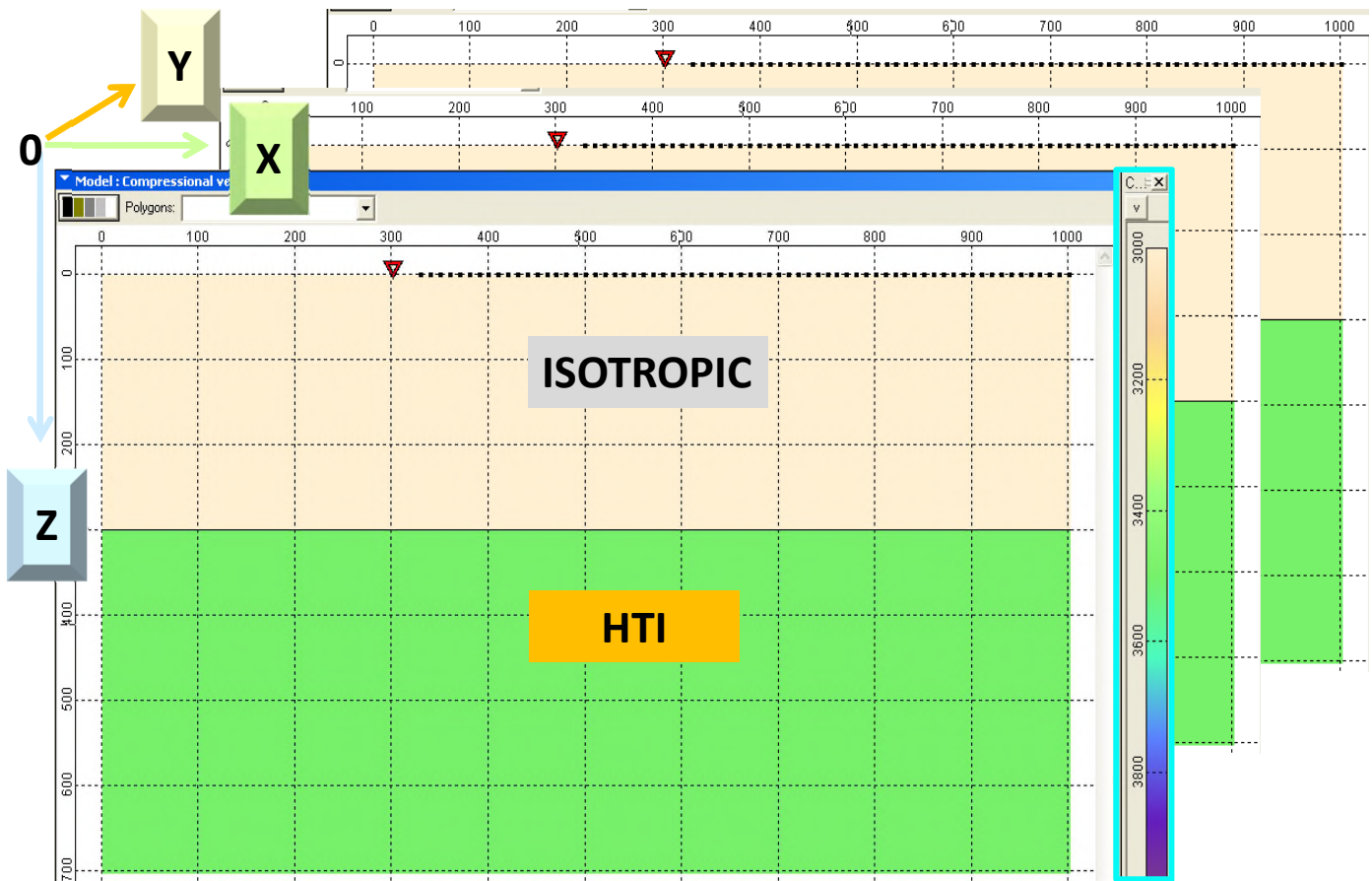
The polarization of qP, qSV and qSH waves in HTI medium and the direction of wave propagation. The plane of fracture is indicated by light-blue color

Apart from the “usual” P and S_2 waves, the S_1 waves also appear, as a result of shear-wave splitting in HTI media, which is here illustrated.

\mathbf{n} is direction of the wave propagation. The fracture plane matches to the Y-Z plane. \mathbf{U}_{qP} is the polarization vector of the qP wave. qSH wave is polarized in the fracture plane, and it is perpendicular to the polarization vector of the qP waves.

Accordingly, the non-zero component appears, i.e. the S_1 waves. The S_2 wave is polarized along the direction, which is perpendicular to the plane formed by polarization vectors of the qP and S_1 waves, and therefore it is not always perpendicular to the fracture plane.

□ 2-Layer model with the lower HTI layer

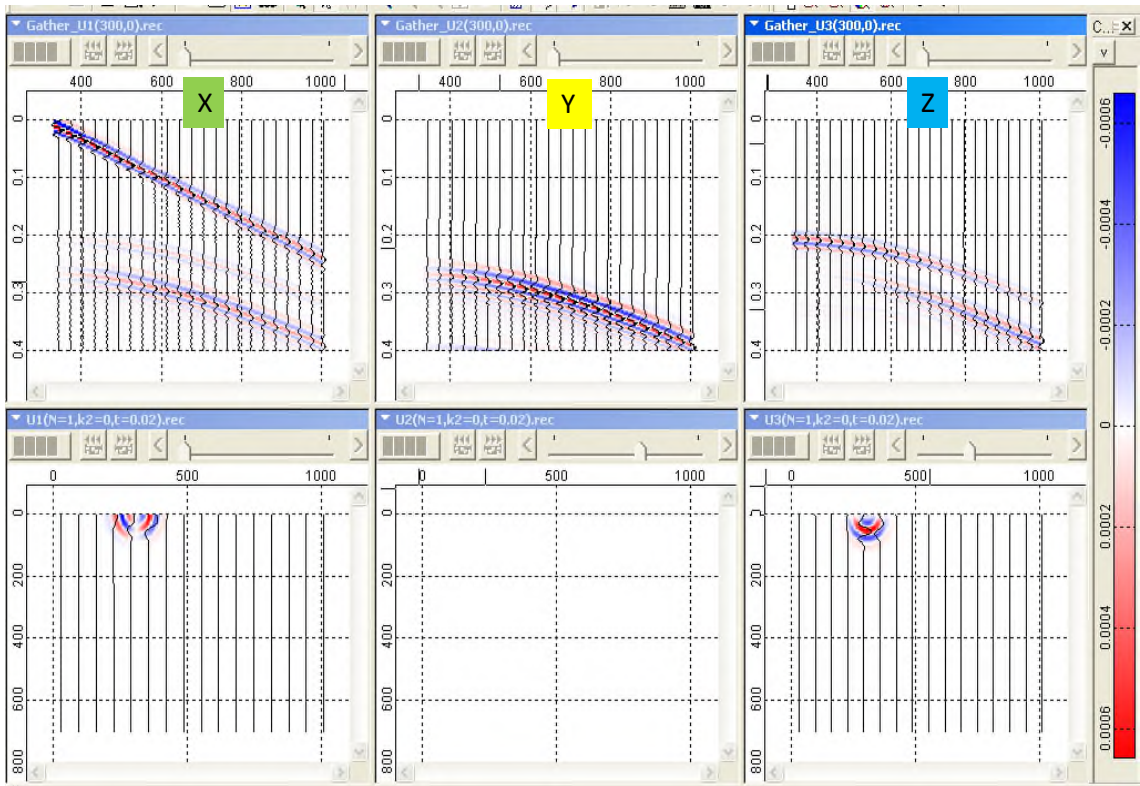


A 2-layer 2.5D model. The upper layer is isotropic and the lower one is horizontal transverse isotropic (HTI). Red triangle and black dots indicate the source and receiver location.

2-layer 2.5D medium is shown: upper layer is isotropic and lower layer is HTI (horizontally transversal isotropic). HTI medium is usually associated to the uniform vertical fracturing and produce the azimuth-dependent seismic anisotropy. This kind of model is most widely used in the practical 3D-3C works now.

At the boundary of the HTI medium, if the source-receiver orientation is not parallel to the fracture plane or perpendicular to the fracture plane, then the birefringence will occurs, i.e. the two converted waves, i.e. P-SH and P-SV appear. The first one is always polarized in the plane formed by polarization vectors of the pseudo-P wave and it is named as the fast converted wave, and the second one is polarized in the plane perpendicular to the plane formed by polarization vector of the pseudo-P and it is named as the slow converted waves. In this slide, the fracture within the lower layer is oriented along the angle 45° with respect to the profile orientation.

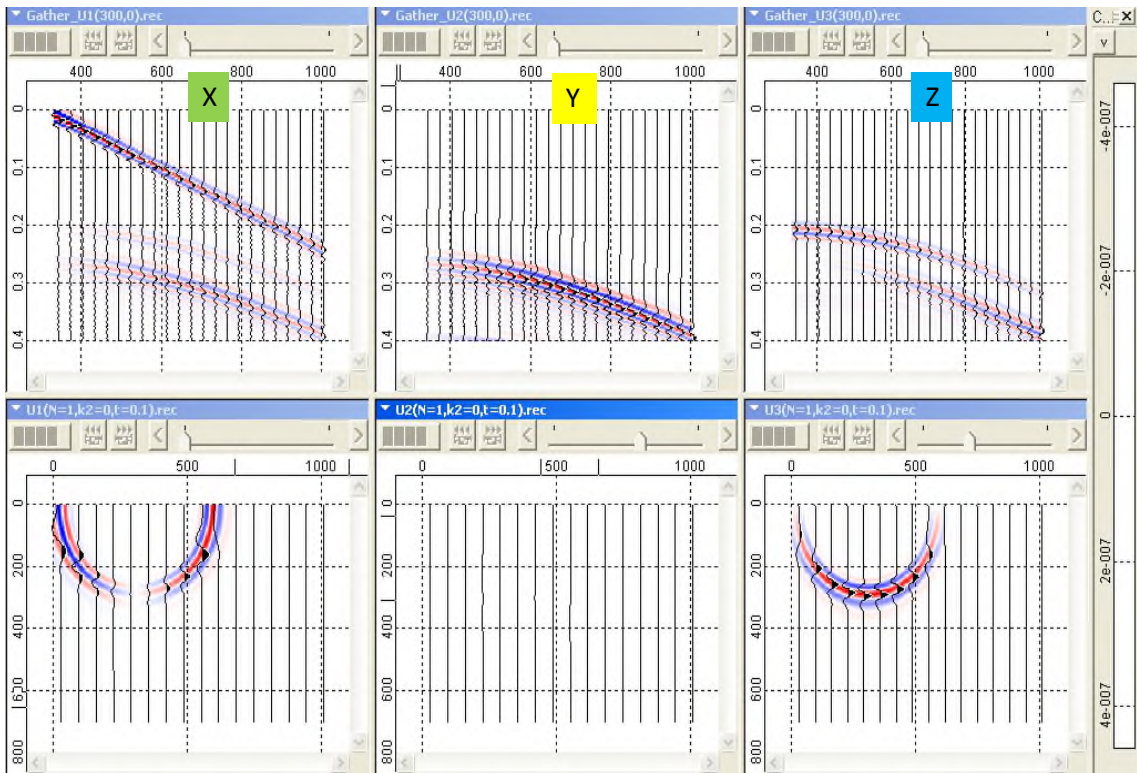
2-Layer model with the lower HTI layer



Shotgathers (upper) and snapshots at $t=0.02$ s (lower) for X (left), Y (middle) and Z (right) component

The 3-component gathers recorded by receivers along the X axis are shown in the upper part. The corresponding snapshots at time of 20ms are shown below. Since the upper layer is isotropic, there is no birefringence. This is the reason why Y-component is null.

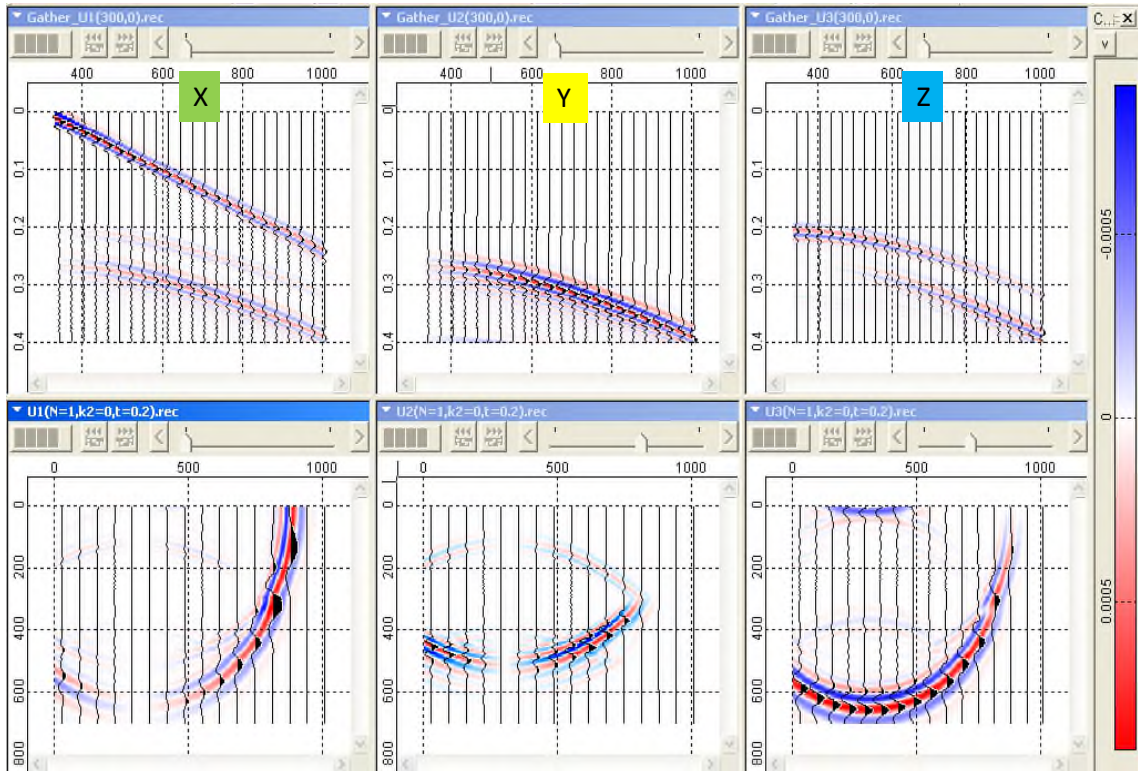
2-Layer model with the lower HTI layer



Shotgathers (upper) and snapshots at $t=0.10$ s (lower) for X (left), Y (middle) and Z (right) component

The wave has reached the boundary at time of 100ms, but not yet reflected.

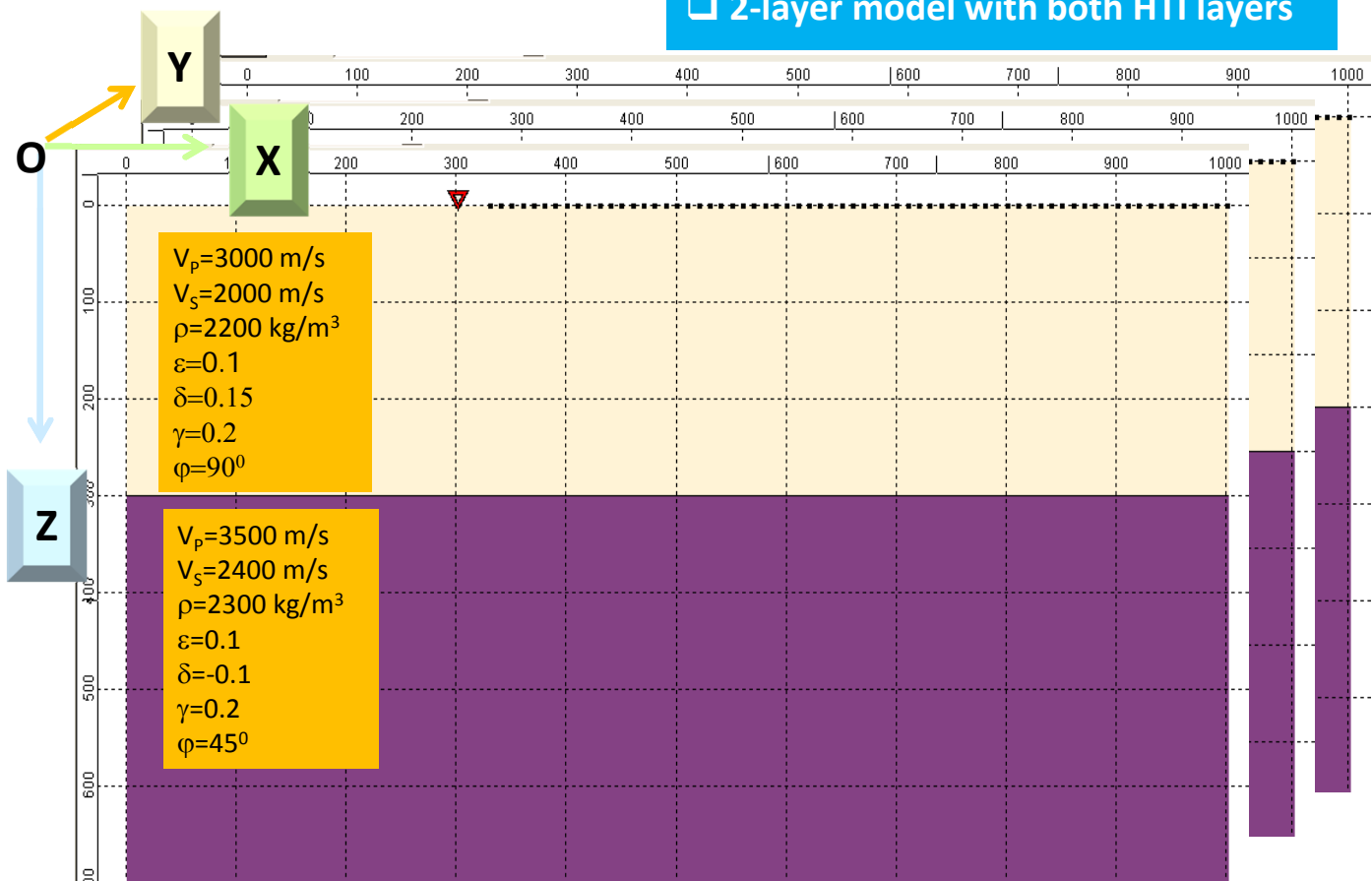
2-Layer model with the lower HTI layer



Shotgathers (upper) and snapshots at $t=0.20$ s (lower) for X (left), Y (middle) and Z (right) component

The wave-mode conversion or birefringence happened at the anisotropic interface. The reflected P-SH wave was generated in the isotropic area and is recorded in the Y component. In addition, the transmitted qP-qSH wave was generated in the lower layer. Also the converted P-SV wave appeared. Because the upper layer is isotropic, the P-SH and P-SV velocities are equal, as seen in the X and Y components of the 3C gathers.

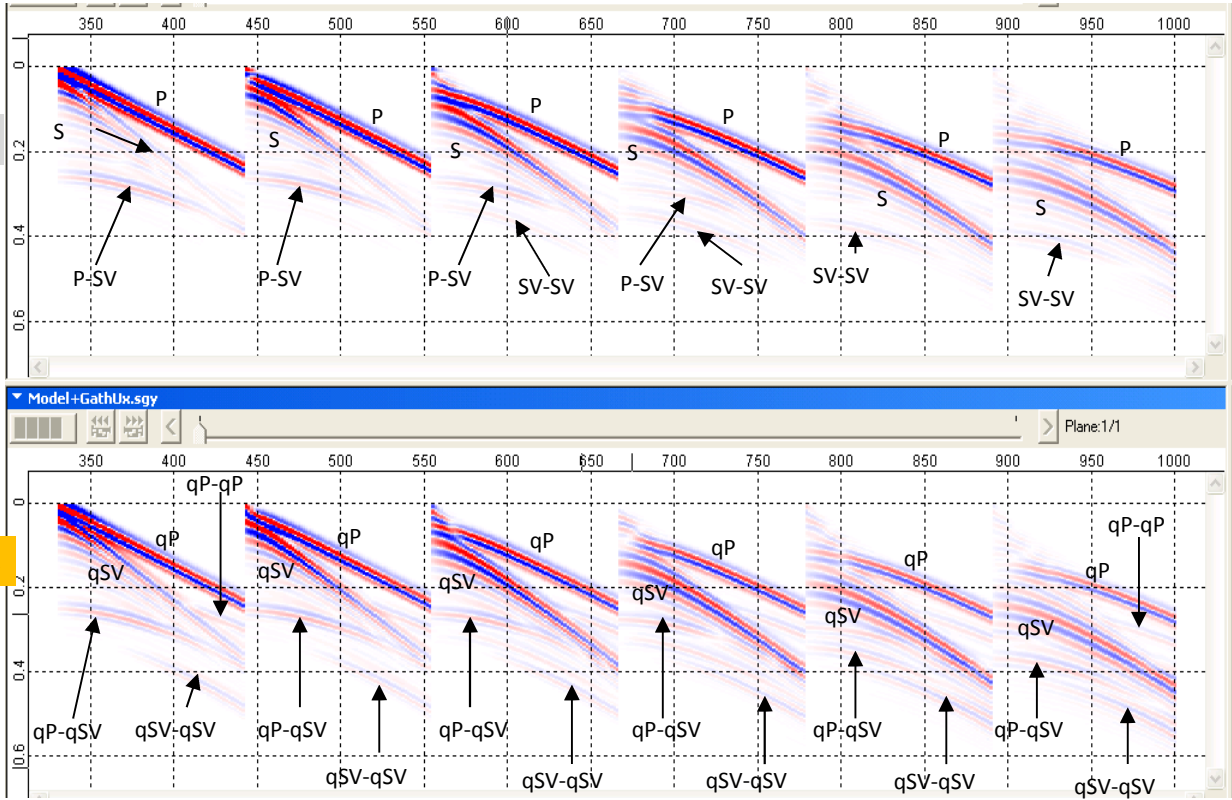
2-layer model with both HTI layers



2-layer anisotropic model with the velocities shown in the yellow box. Red triangle and black dots indicate the source and receiver location.

To make the model a bit complex, both the upper and the lower layers are HTI. In the upper layer as it is shown. In the upper layer, the fracture plane is perpendicular to the source-receiver direction. In lower layer, the symmetry axis of HTI are rotated by 45 degrees relative to X-axis (source-receiver direction).

Y=0 Y=100 m Y=200 m Y=300 m Y=400 m Y=500 m

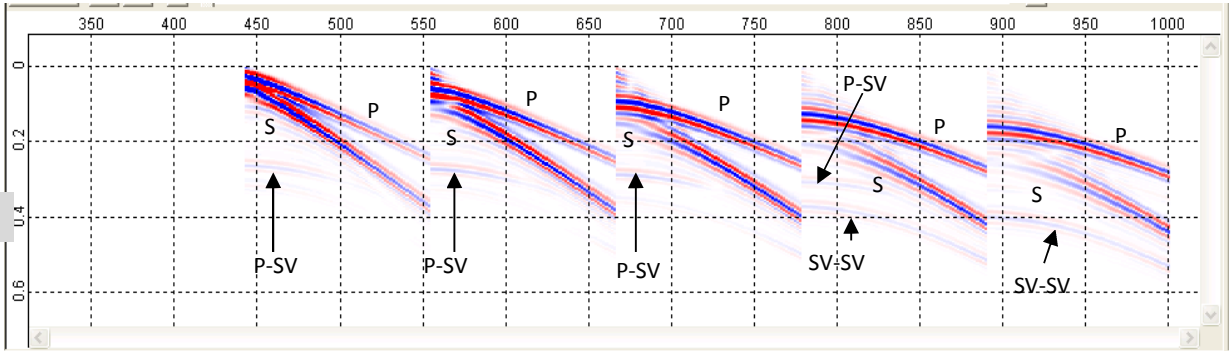


X-components of shot gathers for different transverse offset (Y), for the case of isotropy (upper) and anisotropy (lower).

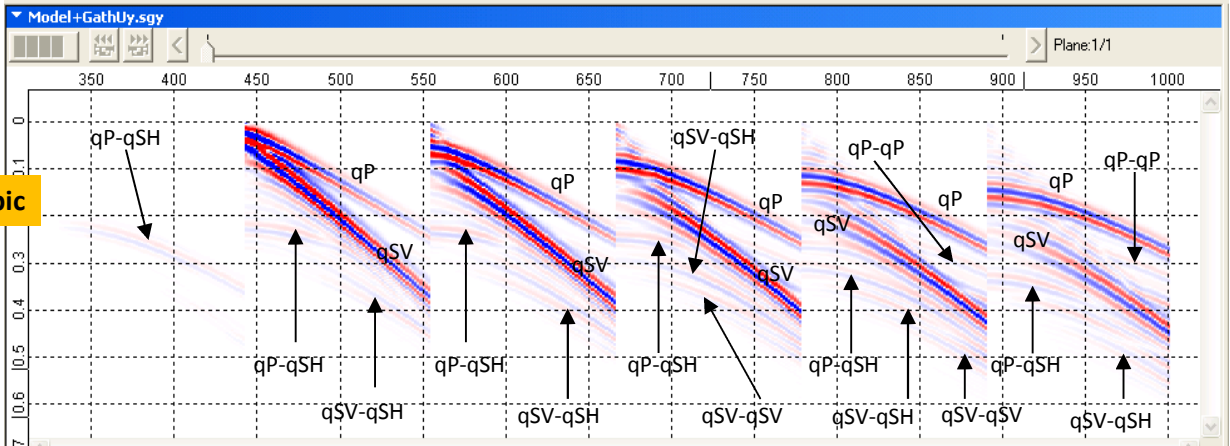
As mentioned above, an important feature of the 2.5D modeling is to model the 3D layout of receivers (wave propagation in 3-D space). Shown is the X component of a shot gather for different crossline offset (Y offset or transverse offset). In the upper part, the gathers for isotropic model are shown, and in the lower part is the shot gathers for anisotropic model. It can be noted that, with increasing crossline offset, the direct wave become more and more hyperbolic, as is expected. In case of an anisotropic model, the gathers contain far more types of waves because of complex wave-mode conversion in anisotropic media.

2-layer model with both HTI layers

Y=0 Y=100 m Y=200 m Y=300 m Y=400 m Y=500 m



Isotropic

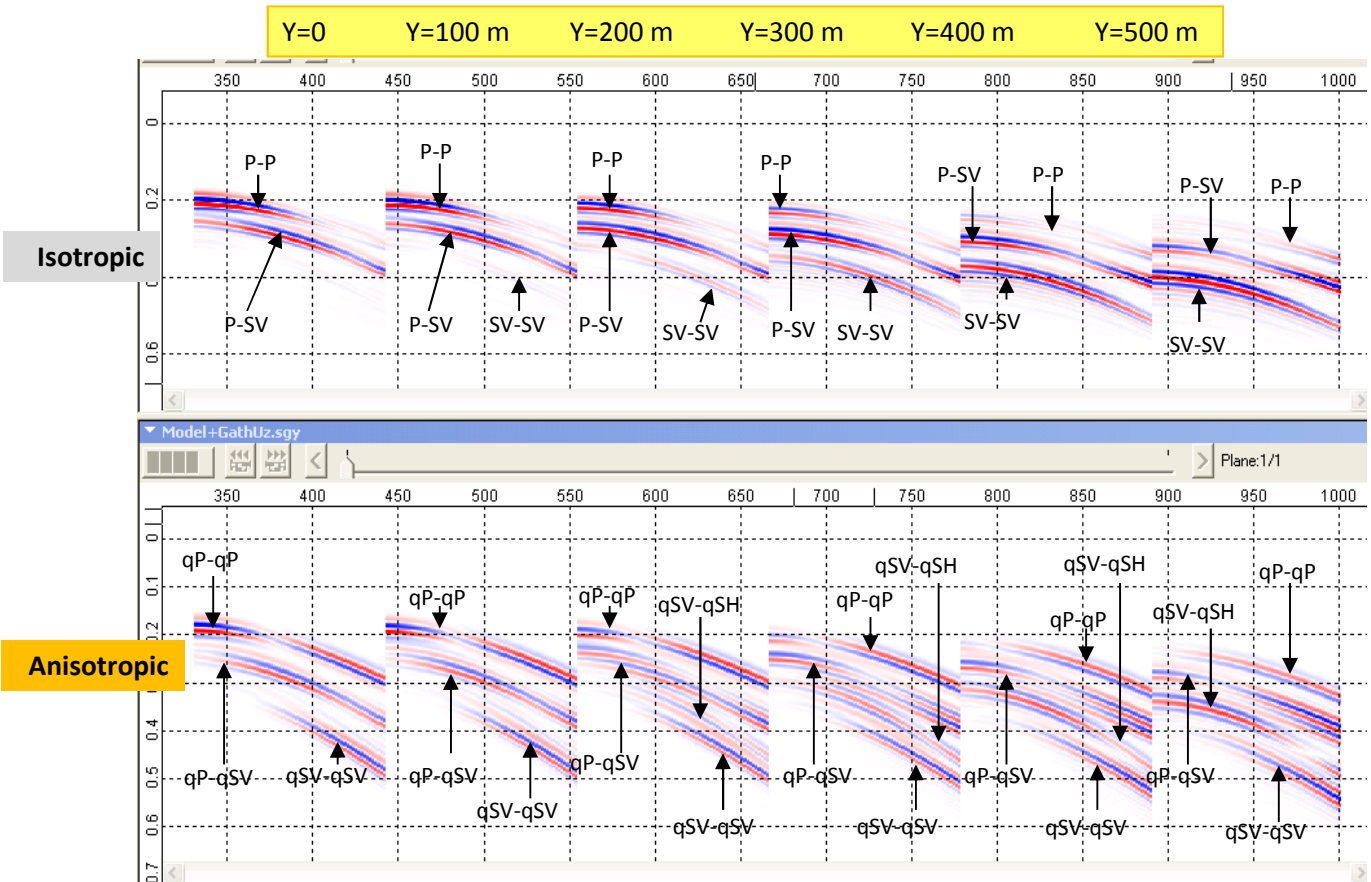


Anisotropic

Y-components of shot gathers for different transverse offset (Y), for the case of isotropy (upper) and anisotropy (lower).

The same observations apply for Y component, as seen here.

2-layer model with both HTI layers

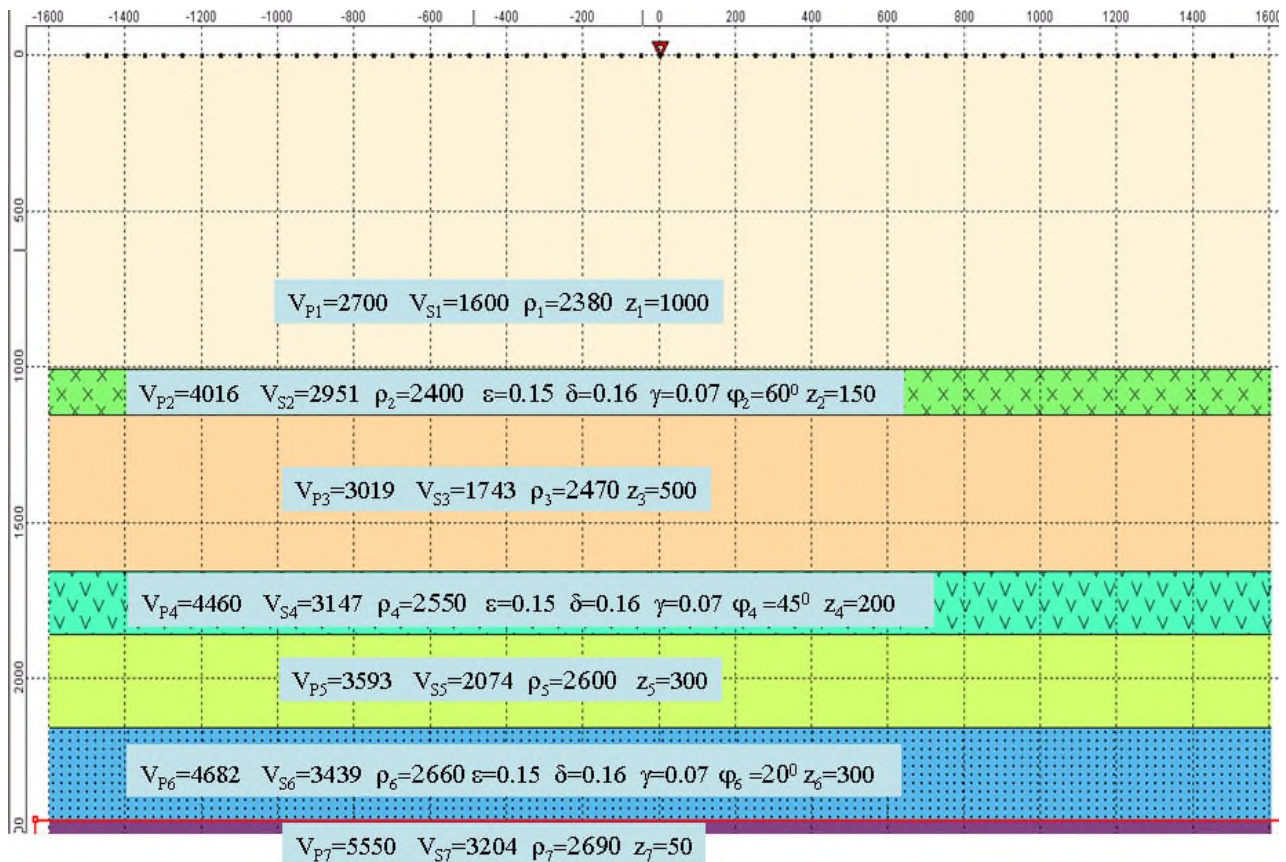


Z-components of shot gathers for different transverse offset (Y), for the case of isotropy (upper) and anisotropy (lower).

In the Z-component, apart from the “usual” P and S_2 waves, the S_1 waves also appear, as a result of shear-wave splitting in HTI media, which is illustrated in **Slide 15**. In **Slide 15**, n is direction of the wave propagation. The fracture plane matches to the Y-Z plane. UqP is the polarization vector of the qP wave. qSH wave is polarized in the fracture plane, and it is perpendicular to the polarization vector of the qP waves. Accordingly, the non-zero component appears, i.e. the S_1 waves. The S_2 wave is polarized along the direction, which is perpendicular to the plane formed by polarization vectors of the qP and S_1 waves, and therefore it is not always perpendicular to the fracture plane.

The 3C wide-azimuth dataset enable determination of fracturing parameters using all types of waves. Particularly, information about the fractures is contained in the direction of the polarization vector, and also in the time delays between the fast and slow shear waves. In practice, the delays between the fast and slow shear waves is the main indicator of fracturing, because the magnitude of this time delay is closely related to the density of fractures and to fluid-saturation in the fractures. However, The inversion of fracture parameters from shear-wave splitting could be complicated by several factors: 1) presence of several fractures at different depths; 2) small thickness of the fractured zones; 3) the area of fracture zone may not wide enough and etc. In these cases, the 3D-3C inverse modelling can play a key role to evaluate the possible complications.

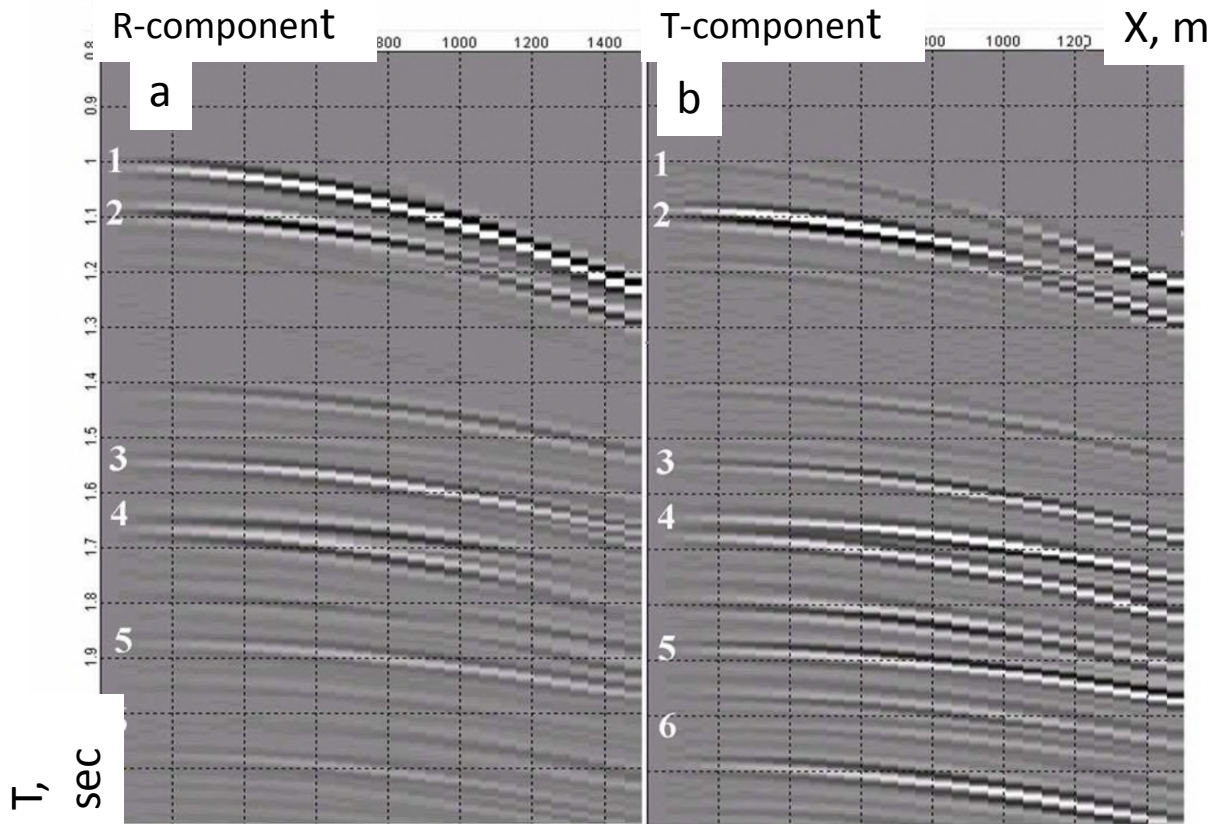
Multi-layered isotropic-HTI model



Multi-layered HTI model with Thomsen anisotropic parameters shown for each layer

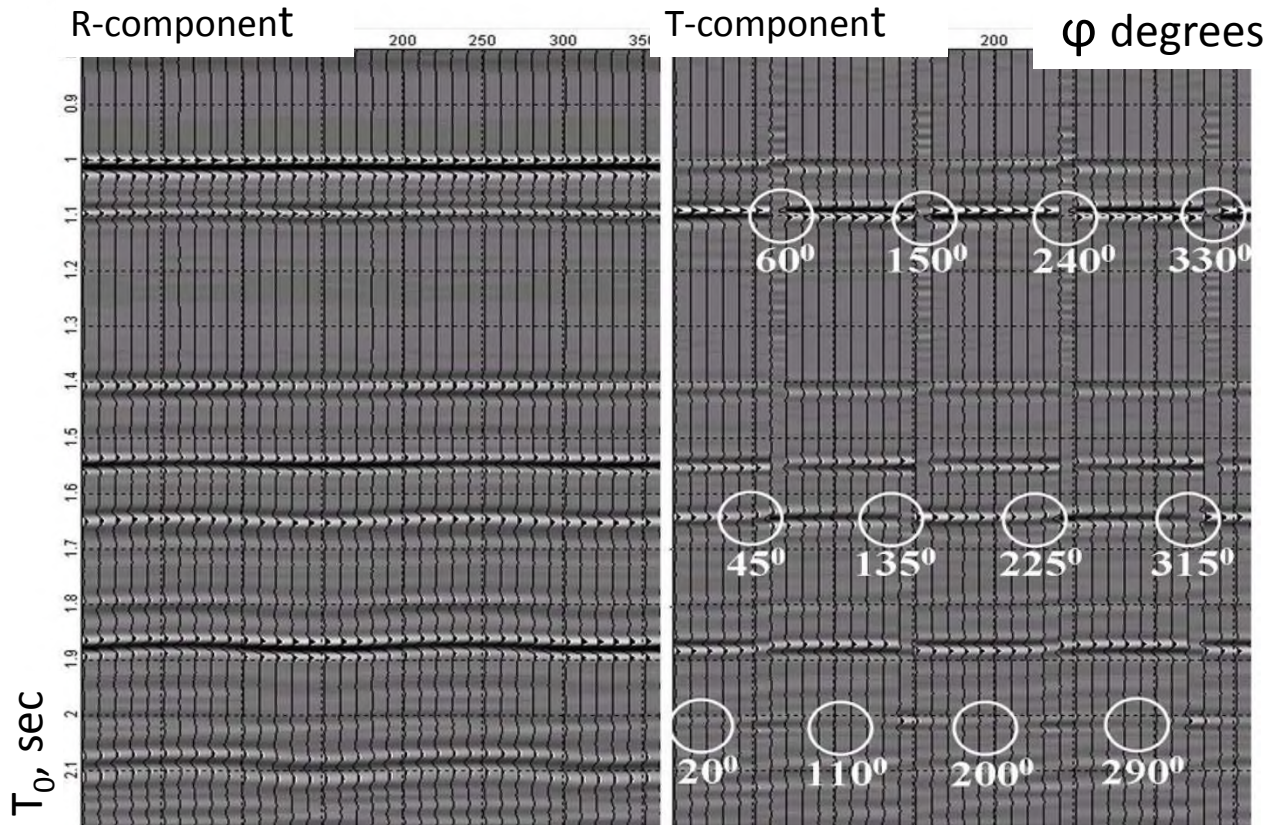
Let's demonstrate it using the model shown here.

The model consists of 7 layers, 3 of which are HTI layer.



Shot gather at azimuth 90° . Only converted waves(left), all types of waves (right).

The two synthetic gathers are shown in the Radial-Transverse coordinate system. The numbers show the reflected converted waves from the top and bottom of each HTI layer.

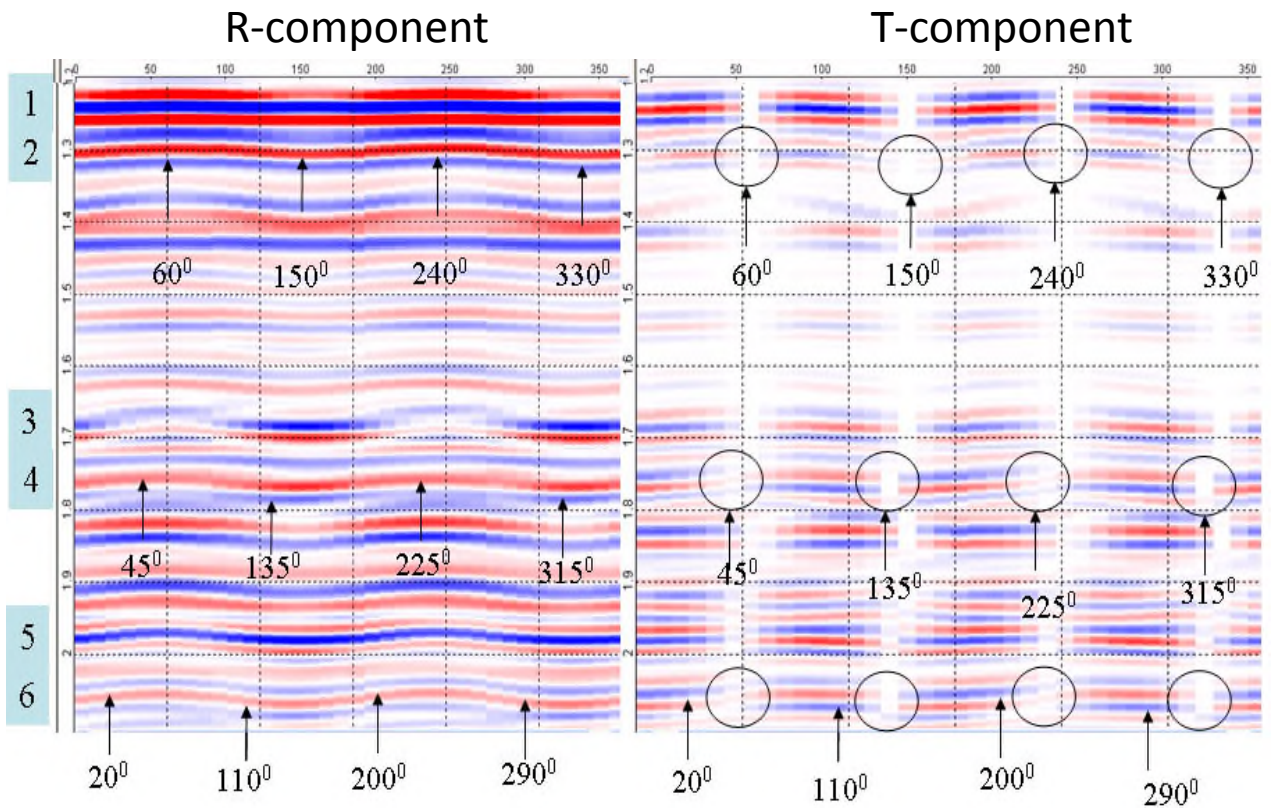


Azimuthal CDP stacks of radial component (left) and transverse component (right), after applying the layer stripping of anisotropic effects.

For the azimuthal processing of the horizontal components, we first need to obtain the Radial (along the source-receiver line) and Transversal components (perpendicular to the source-receiver direction) of the wavefield. Then, the other processing steps of the horizontal components consist of:

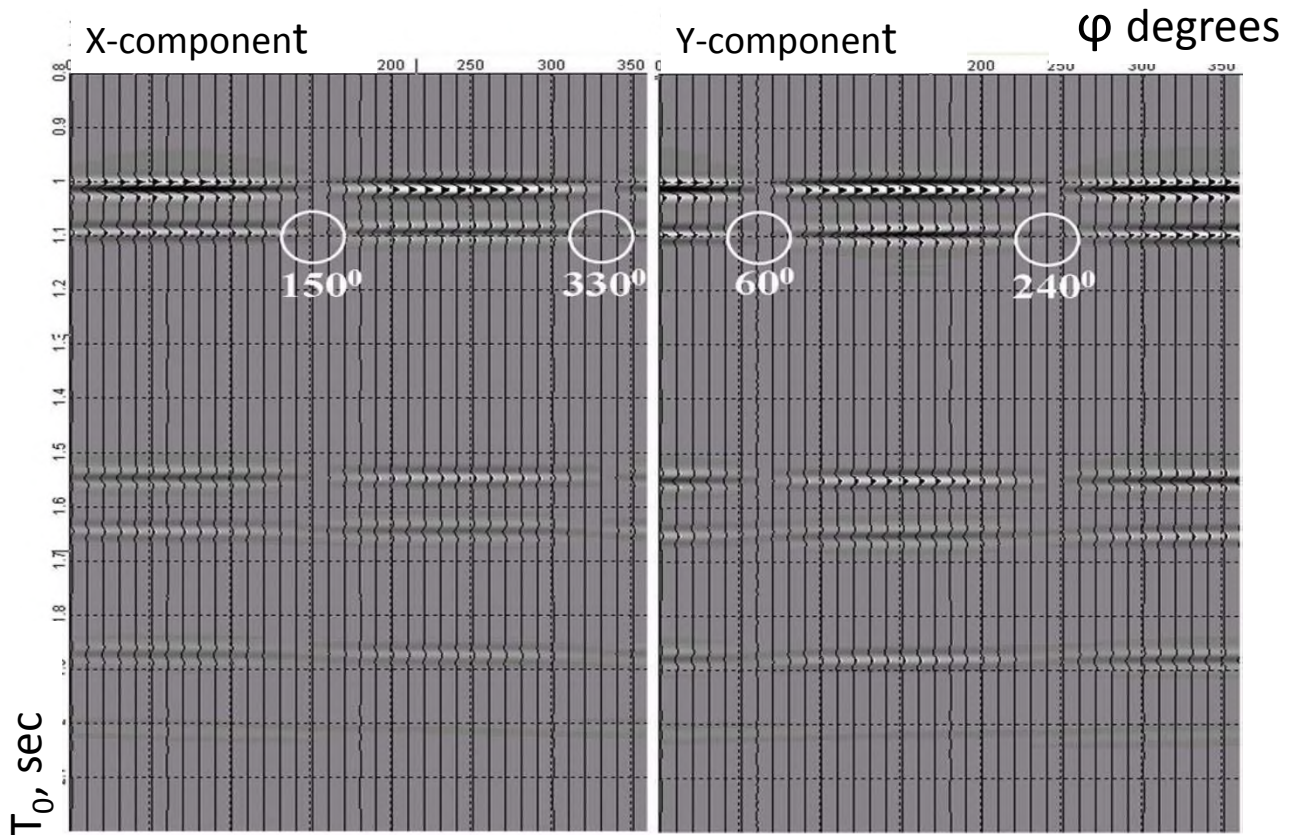
- Obtain the azimuthal stack in the R-T coordinate system.
- Determine the natural coordinate system for the first anisotropic layer.
- Determine the time delays between the fast and slow quasi-shear waves for the first anisotropic layer from the azimuthal stack.
- Layer-by-layer stripping of the effect of velocity differences in the overburden anisotropic layer (known as layer stripping method)
- Evaluate the time delays between the fast and slow quasi-shear waves for the second anisotropic layer from the azimuthal stacks

The CDP azimuthal stack is shown. The zeroes of the T-component indicate azimuths, where the qSH wave is absent. In case of only one HTI layer, these azimuths indicate the plane of the vertical fracturing accurate up to 90 degrees, and the extrema of the R-component correspond to the zeroes of the T-component and determine the orientation of the fracture uniquely. The time differences between 2 mentioned extrema in T- and R-component is proportional to the density of fractures. The larger this difference is, the higher is the density of fractures.



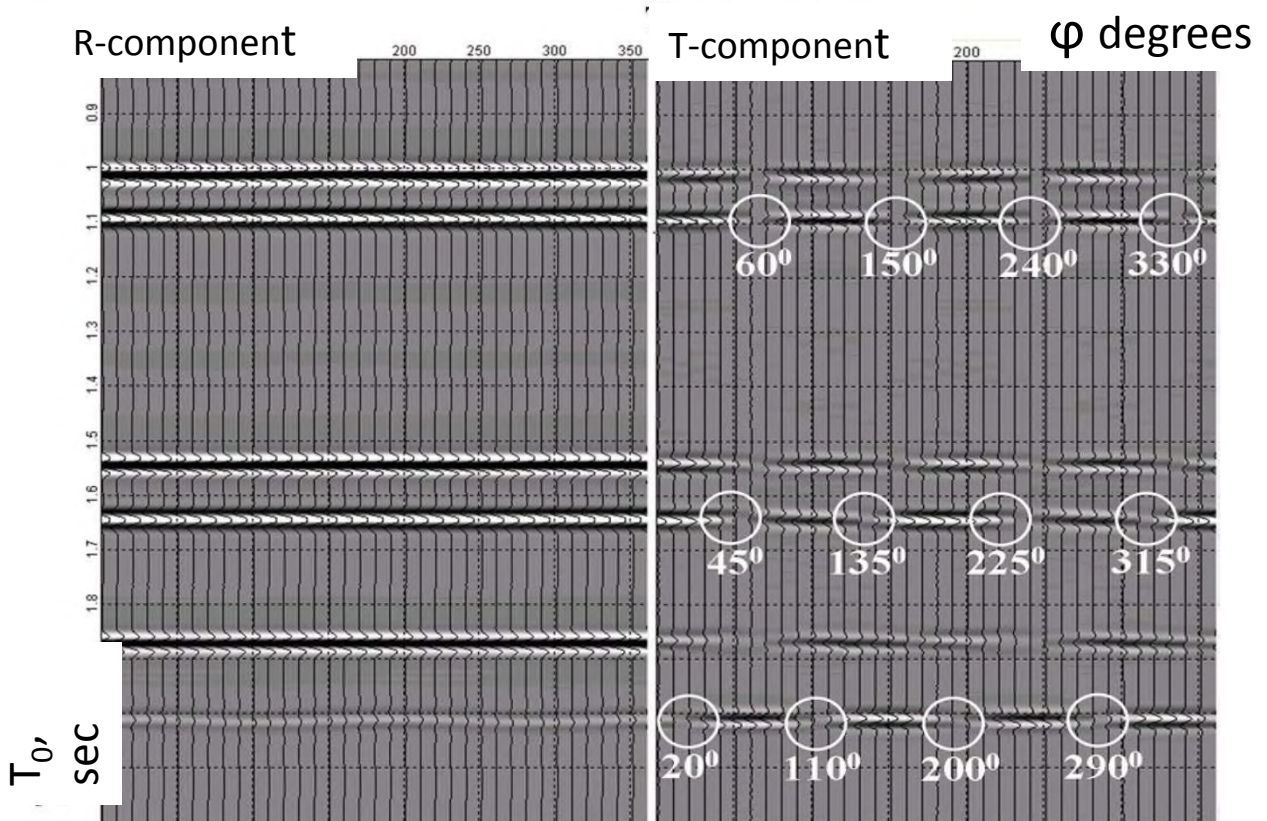
Azimuthal CDP stacks of radial component (left) and transverse component (right) without applying the layer stripping of anisotropic effects

However, here it can be seen that the zeroes of the T component, especially for the 3rd anisotropic layer, are biased away from the true natural coordinate system. For the upper layer, the zeroes are closer to the natural coordinate system. The difference between the times of the fast and the slow waves cannot reflect reliably the density of fractures.



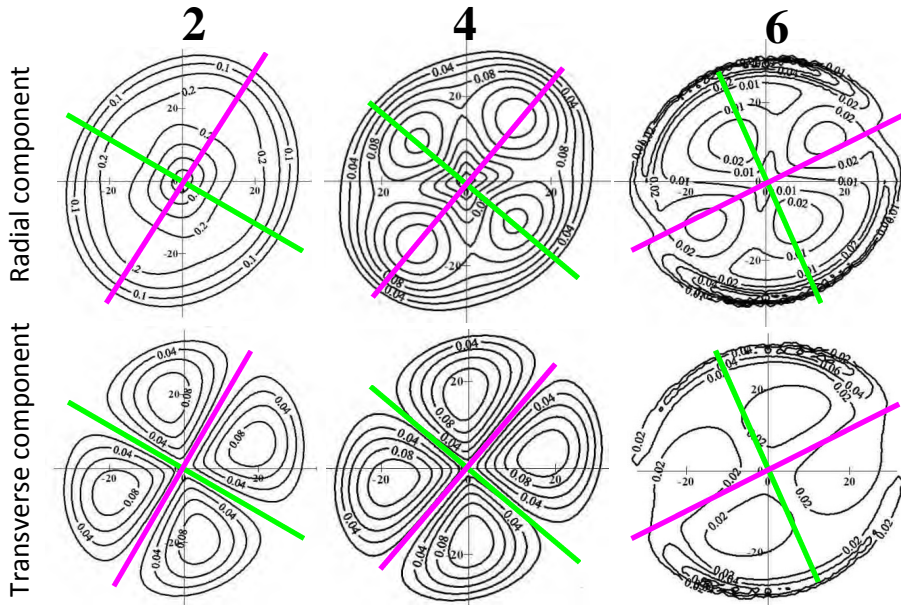
Azimuthal CDP stack in natural coordinate system for second layer

In this case, layer stripping should be used. In this picture, the azimuthal stacks are shown in the natural coordinate system for the 2nd layer. The layer stripping enables to remove the effect of fast waves and the slow waves of overburden layers, and then reduce these waves to the same time at the level of the target layer, using the static corrections. After that, re-calculation of horizontal components to the R-T coordinate system is carried out.



R and T components of azimuthal CDP stacks after layer stripping of the anisotropic effect of 2nd and 4th layers

This picture shows an example after stripping the 2nd and the 4th layer. After that, the relation between the time delay at the extrema for the reflections of the 6th layer is not contaminated by the overburden anisotropic layers. So the azimuth of fracture plane can be determined for this layer.



Amplitude variation with azimuth (AVA) of P-S waves reflected from the bottoms of layers for Radial component (upper) and Transverse component (lower). Green line - azimuth of the fracture. Purple line - normal to the fracture

For the AVA analysis, the azimuthal AVA may be formed for the R and the T components for each layer respectively. In this picture it can be seen that the azimuthal AVA has elliptic shape for the R component, and that the ellipse is rotated in accordance to the azimuth of fracturing. The ratio between the short and long axis of the azimuthal AVA ellipse is the most important indicator of the fracture density.

Shale (top)

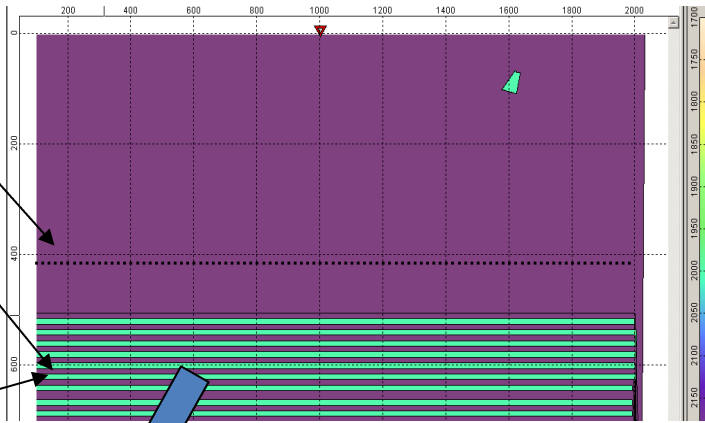
$V_p=2200$ m/s
 $V_s=800$ m/s
 $\rho=2086$ kg/m³

Gas-saturated sandstone $h=10$ m

$V_p=2000$ m/s
 $V_s=1300$ m/s
 $\rho=2010$ kg/m³

Shale thin layers $h=10$ m

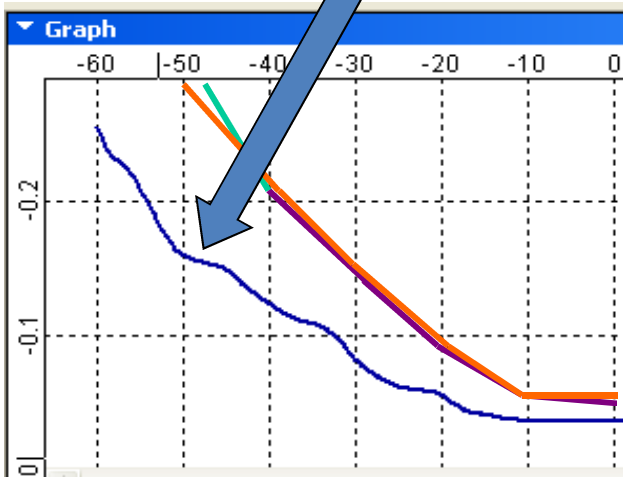
$V_p=2200$ m/s
 $V_s=800$ m/s
 $\rho=2086$ kg/m³



Model with thin-interbedded layer, whose effective anisotropic parameters are:

$V_p=2090$ m/s, $V_s=967$ m/s,
 $\rho=2050$ kg/m³,

$\sigma=0.36$, $\epsilon=-0.052$,
 $\delta=-0.118$



Comparison of AVO graphs for two-layered, three-layered and multilayered models with a 20Hz Ricker wavelet .

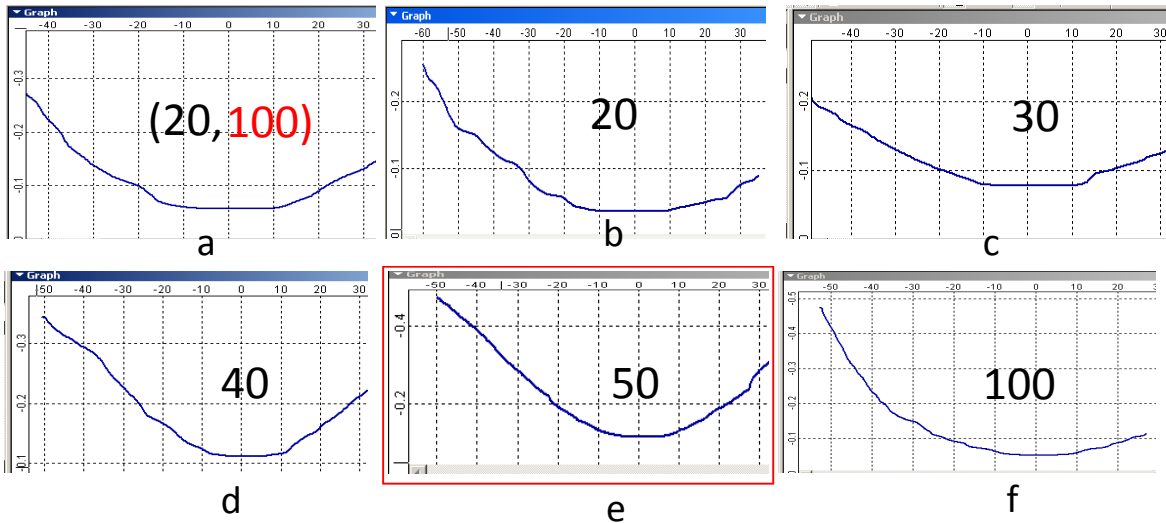
Legend:

- Thin-layered pack, composed from thin layers (10 m), parameters of which correspond to Ostrander model
- Two-layered Ostrander model
- Three-layered medium composed from sandstone layer with 10 m thickness immersed into shale. Sandstone and shale parameters correspond to Ostrander model.

In *this Slide*, the AVO curve for the 2-layered Ostrander model (yellow line), for the 3-layer model (green line) matches to each other at the signal frequency of 20 Hz.

The blue line shows the AVO curve for the multi-layered medium for the same signal frequency, which is obviously different from the AVO curve obtained for the 2-layer and 3-layer models.

The latter AVO curves give the Poisson ratio of 0.1 in sandstones, but in case of the thin-layered pattern, the inverted Poisson's ratio becomes 0.36, which means the absence of gas – whereas it was modelled for each sandstone layer.



Comparison of AVO for different frequencies for thin-layered pack and two-layered model. Significant difference of magnitudes requires application of different scales for graphics. The highest gradient is observed at peak frequency 50Hz, which corresponds the resonance frequency of the given pack. Next extremum, which have smaller amplitude for the given form is observed at peak frequency 100Hz.

a– two-layered model peak frequency 20Hz. **b** – multilayered model at peak frequency 20Hz. **c** - multilayered model at peak frequency 30Hz. **d** – multilayered model at peak frequency 40Hz. **e** – multilayered model at peak frequency 50Hz. **f** – multilayered model at peak frequency 100Hz.

Dependence of the AVO curves on peak frequency is shown in *this Slide*.

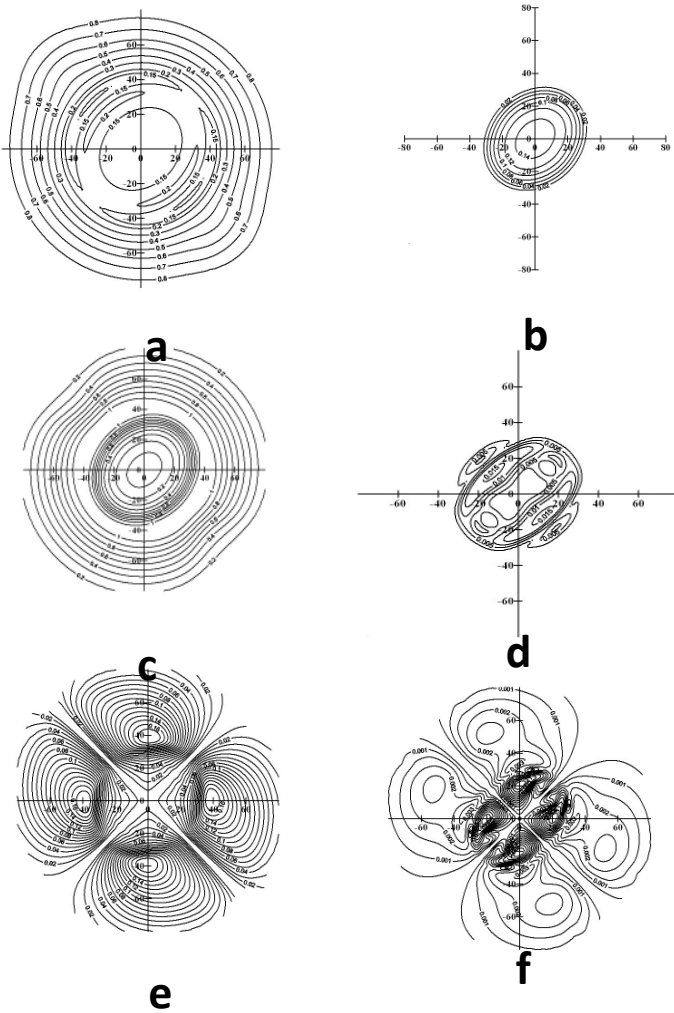
When the peak frequency of Ricker wavelet is equal to 40 Hz, the AVO curve is getting close to the AVO curve of a 2-layer medium from the view of their characteristics.

If the peak frequency of Ricker wavelet is 50 Hz, the strong AVO effect is observed, where the effective Poisson's ratio is falling down to 0.06.

□ Azimuthal AVO and AVOT

It is assumed that clay is VTI anisotropy with Thomson's parameters $e=0.19$, $d=-0.22$, $\gamma=0$, while the sandstone is an inelastic HTI medium with a same quality factors for compression and shear waves: $Q_p=Q_s=10$. The sandstone has a vertical gas-saturated fracturing with an intensities of $DN=0.55$ and $DT=0.25$ (Bakulin et al., 2000). The fracturing has an azimuth of 45° .

(a) qP-qP reflection coefficients;
 (b) qP-qP transmission coefficients;
 (c) qP-qSV reflection coefficients;
 (d) qP-qSV transmission coefficients;
 (e) qP-qSH reflection coefficients;
 (f) qP-qSH transmission coefficients.

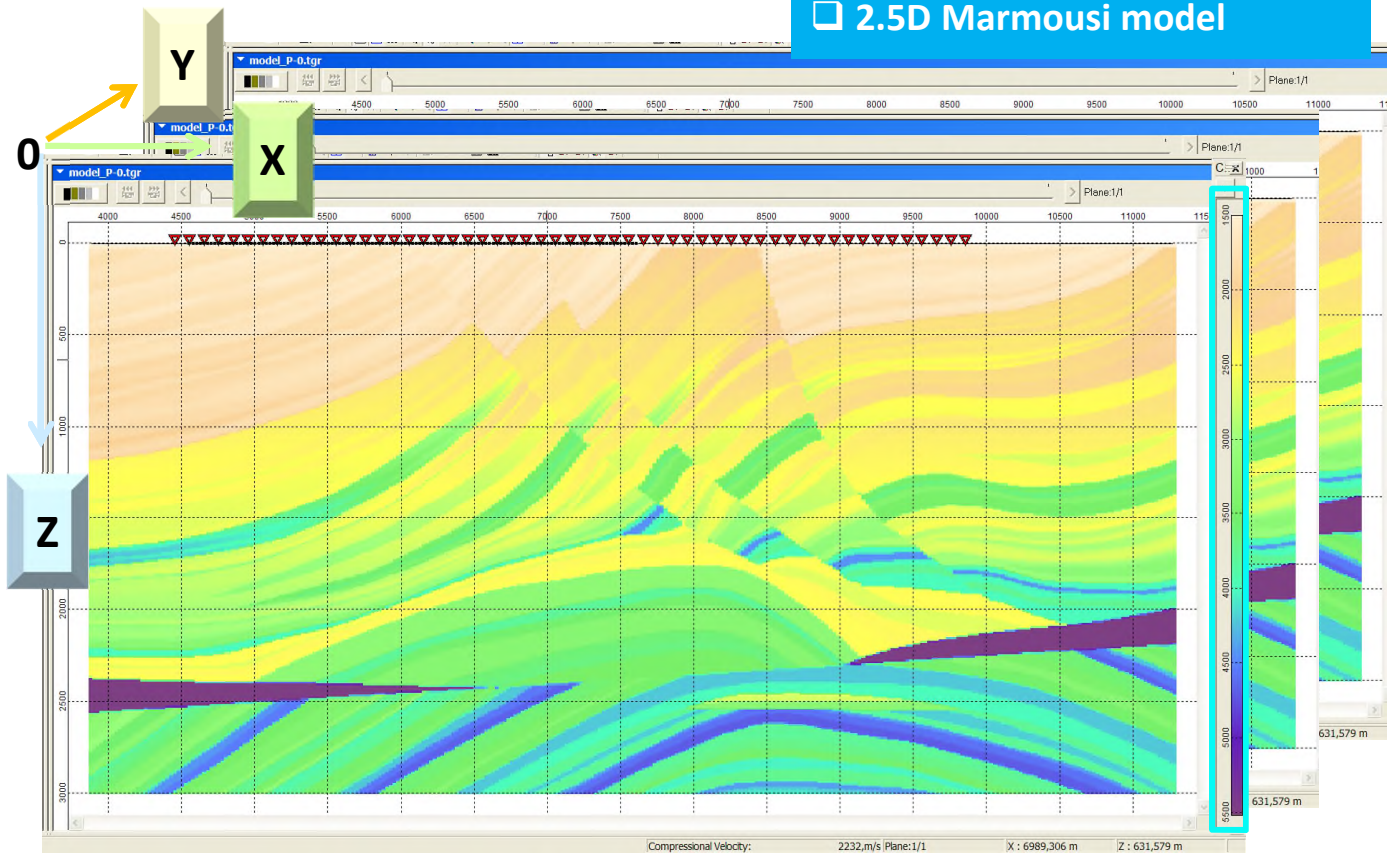


To make the thin-layer model more complicated, we assumed that the clays are VTI-anisotropic, and the sandstones have vertical fracture with absorption $Q_p=Q_s=10$.

In *this Slide*, the azimuthal AVO for such pattern is shown for the reflected (left) and transmitted waves (right) of the qP- waves (upper), qSV- waves (middle), and qSH-waves (lower), where Ricker wavelet with a peak frequency of 30 Hz is used. It could be seen that the the azimuthal dependency for the qP-qSH wave is far more complicated than for the qP- qSV wave.

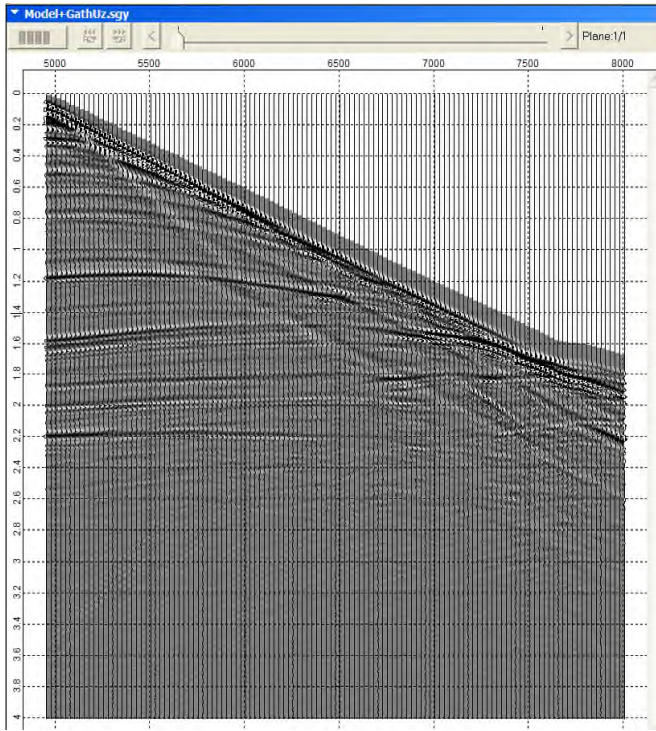
The orientation of the ellipse varies depending on the source-receiver distance (offset). For some offsets, the ellipse is turning into circle. This observation must be taken into account in planning the 3D wide-azimuthal survey.

It also show that, in real conditions, the ellipticity of P-waves AVO is far less obvious than the one of qP-qSV waves, and this fact is good evidence of using 3D-3C observation to detect vertical fracturing. Our modelling 3D-3C tool enables the evaluation of such effect before expensive field 3D-3C or wide-azimuthal 3D-1C survey.

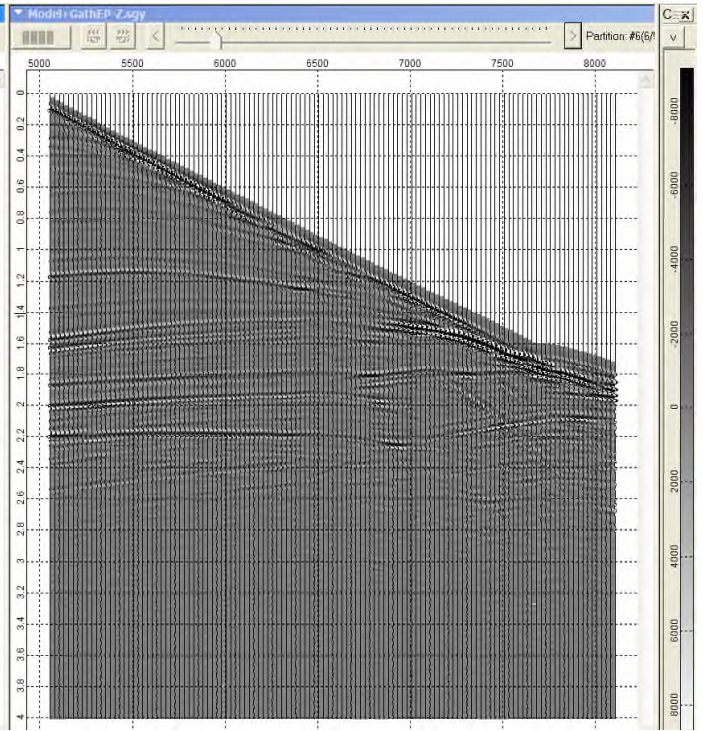


2.5D Elastic Marmousi Model

The 2.5D modeling may be also used for more complicated structures. In *this Slide* the well-known *Marmousi* model is shown.



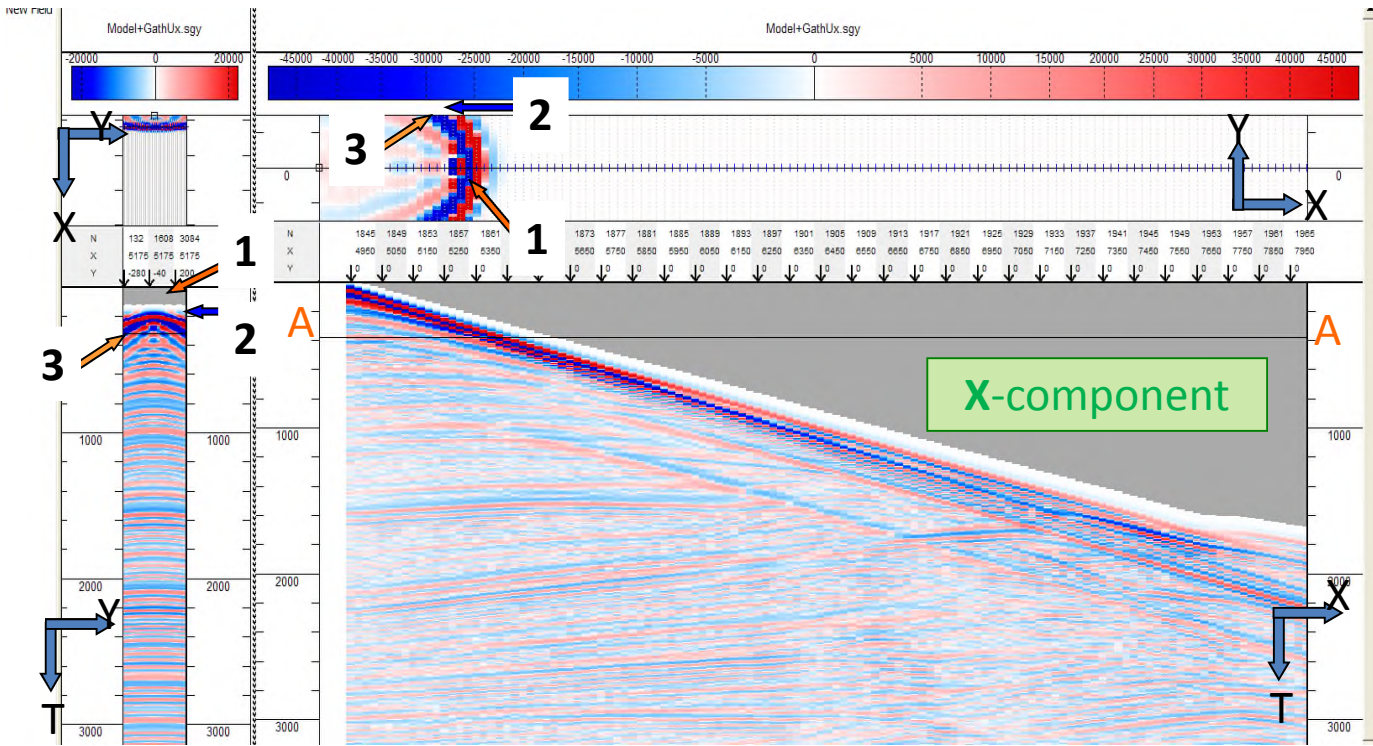
2.5D



2D

Elastic modeling of 2.5D (left) and 2D (right)

One of the gathers obtained for the 2D and 2.5D variants is shown in *this Slide*.

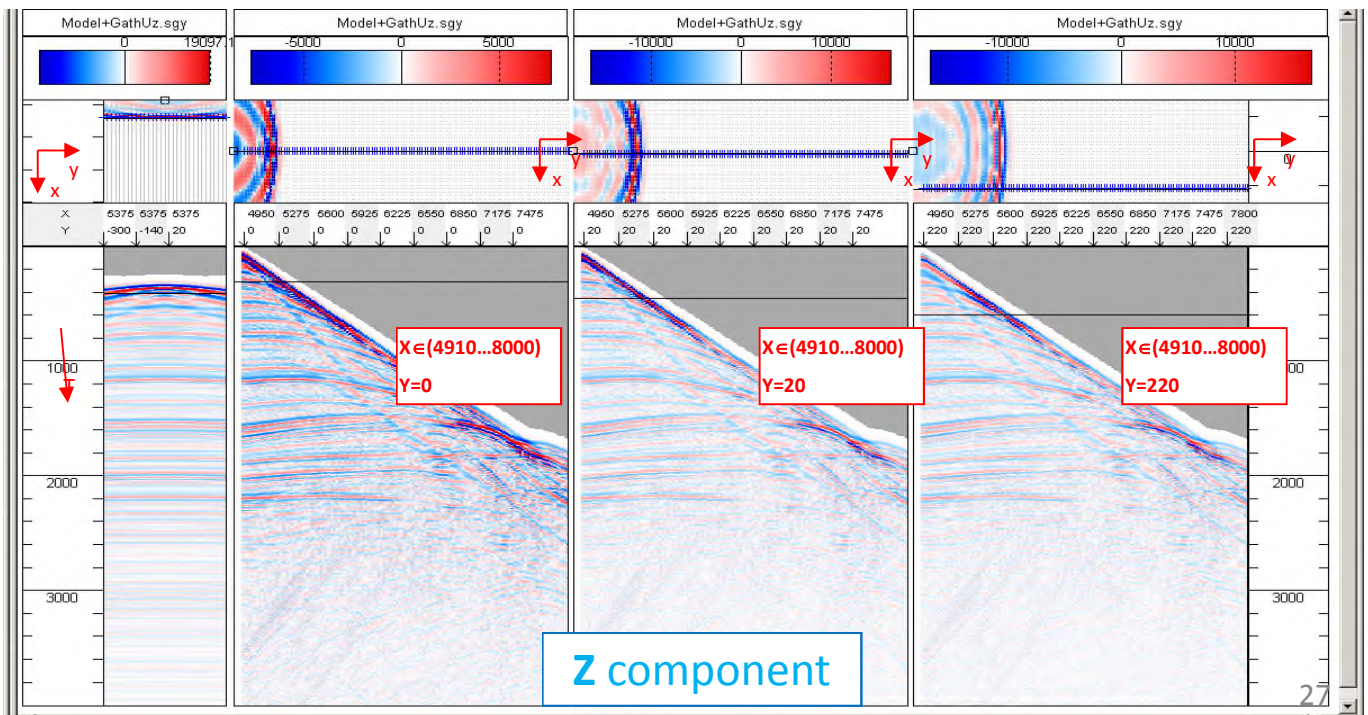
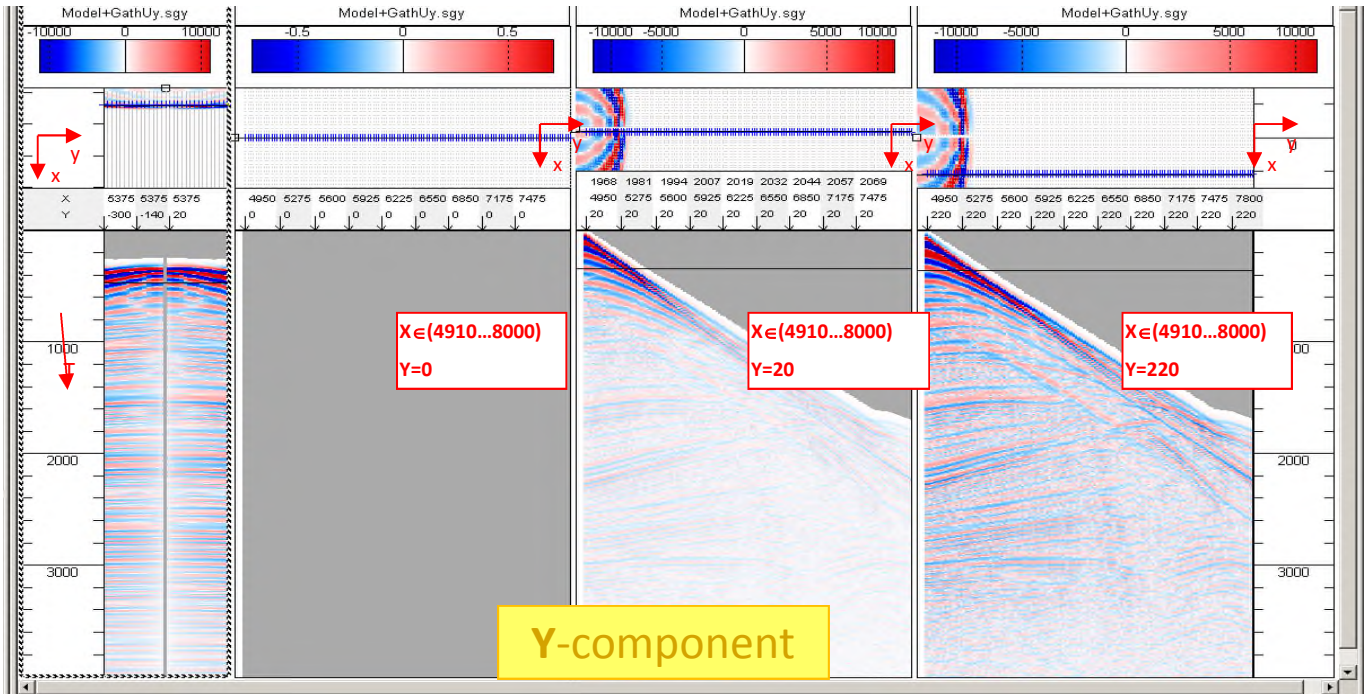


1- refracted wave, 2 - direct wave, 3 – converted wave

AA- level of horizontal slice of 3D shotgather

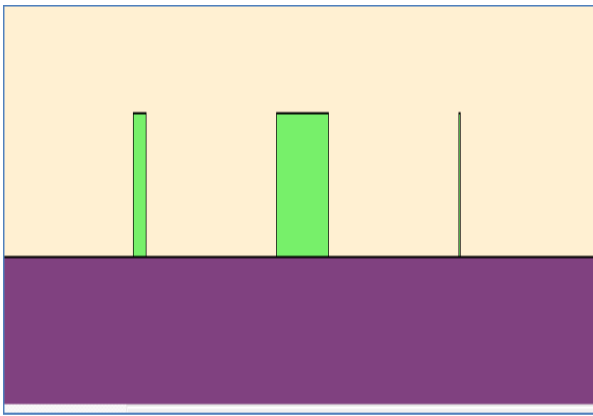
In *this Slide*, the vertical and horizontal sections of 3D gather for X component is shown for shown.

2.5D Marmousi model



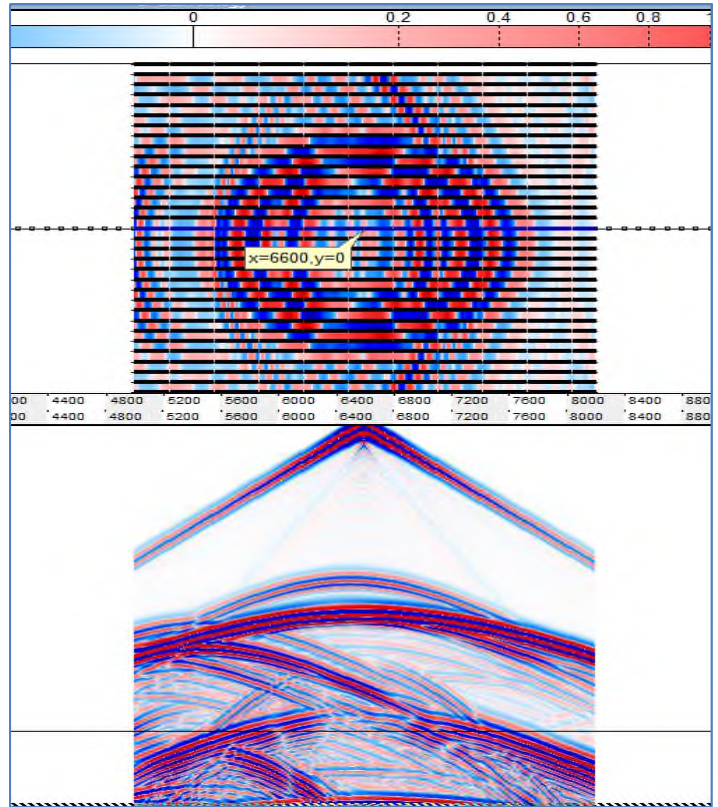
In the *upper and lower Slides*, the Y- and Z-components along different crossline offset (Y offset) are shown, respectively.

□ Model with 3 vertical boundaries



Model with 3 vertical fault zones with thickness of 100m, 400m and 10m, respectively.

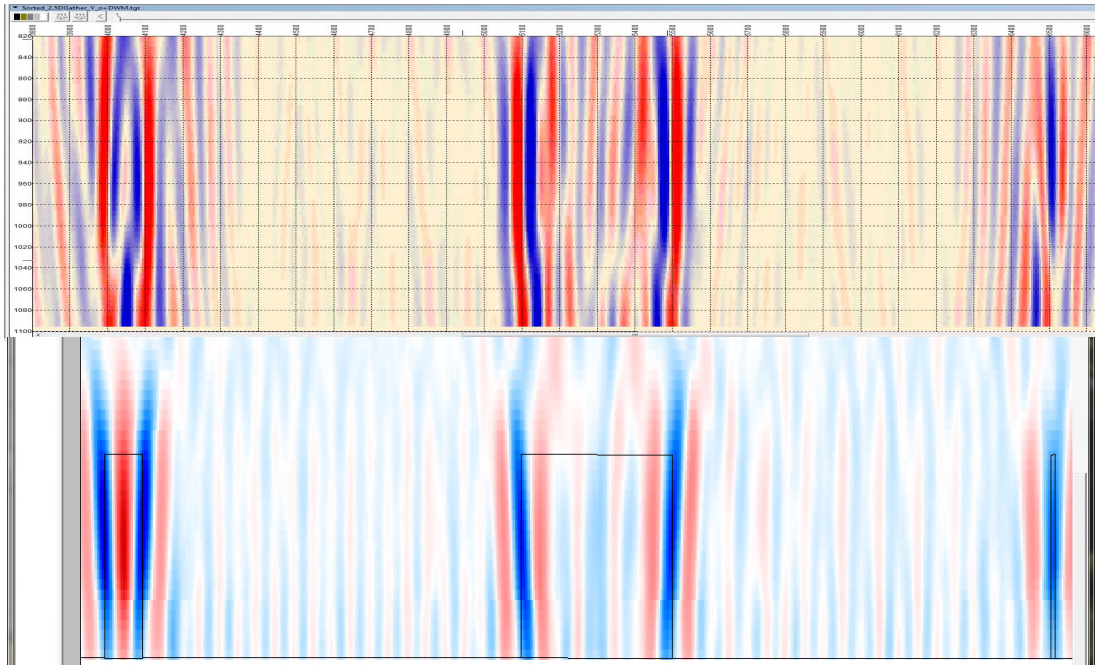
This model is used for the comparison of resolution capability for 2D and 3D processing



3D Synthetic Gather (below) and its time slice at 1200 ms (above).

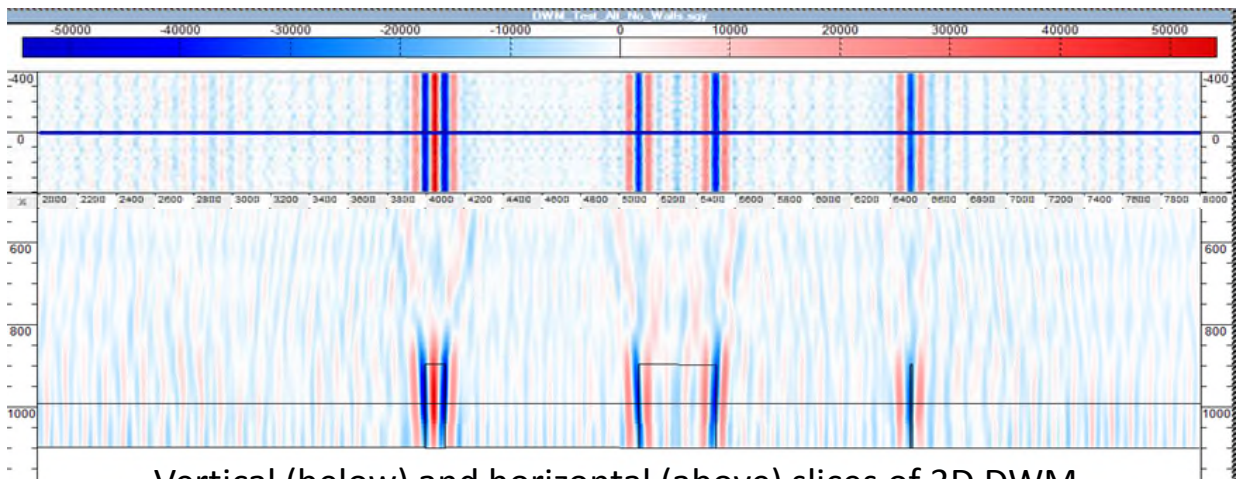
One of the most important aspects of modeling is to evaluate the data processing for various source/receiver layout, including comparison of 2D and 3D processing. In *left Slide*, the model with 3 vertical boundaries with different thicknesses is shown. For this model, the synthetic gathers were calculated in 2D and 3D model respectively.

In *right Slide*, one of 3D shot gathers is shown.



2D DWM (above) and 3D DWM (below). The horizontal resolution of 3D DWM is much better than the 2D DWM

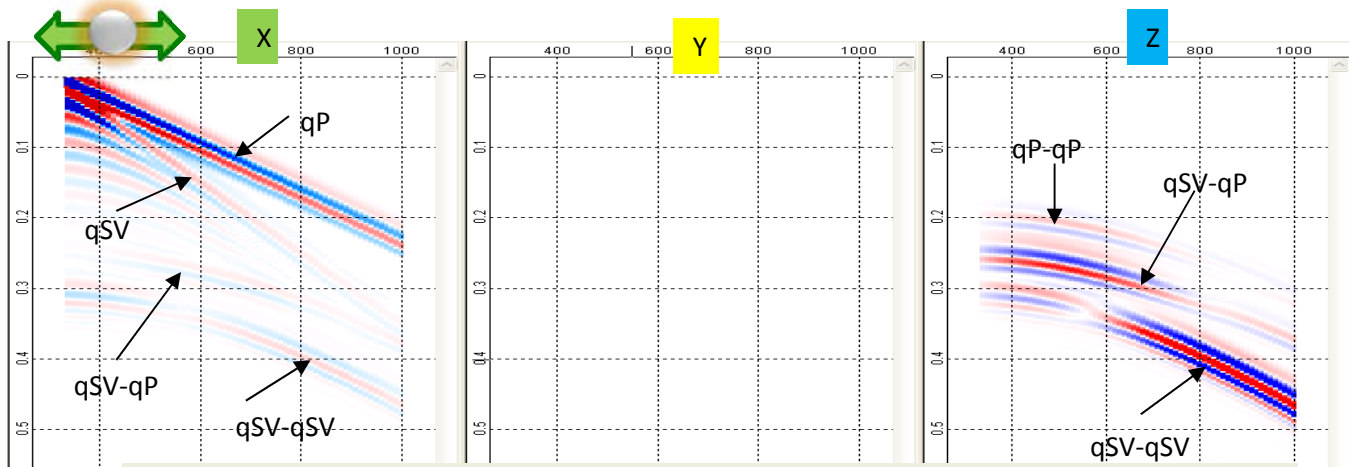
The duplex wave migration is applied for the 2D and the 3D synthetic gathers and the results show that 3D DWM migration has much better horizontal resolution, as shown in *upper Slide*, where the 2D DWM image is shown in the upper part, and the 3D DWM image is shown below.



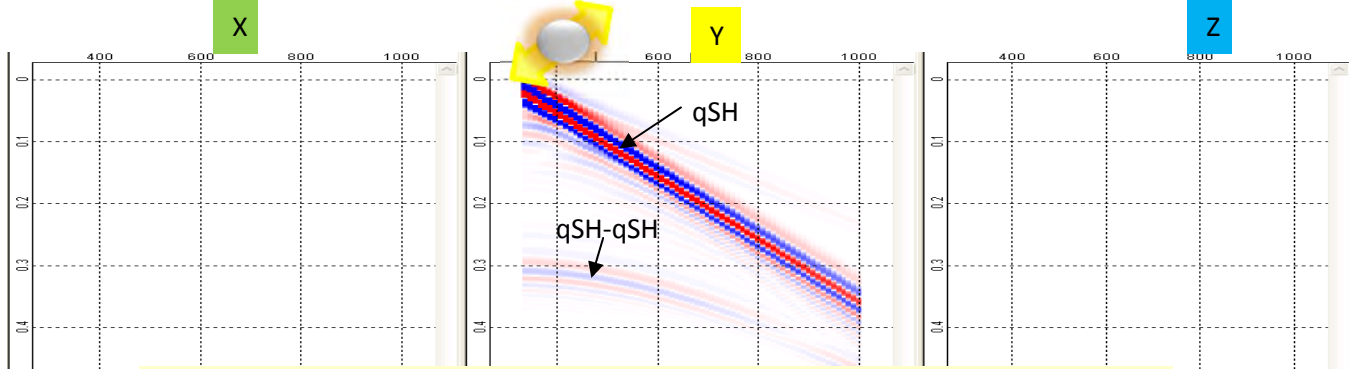
Vertical (below) and horizontal (above) slices of 3D DWM.

In *lower Slide*, the vertical (bottom) and the horizontal (top) slices of the 3D DWM cube are shown.

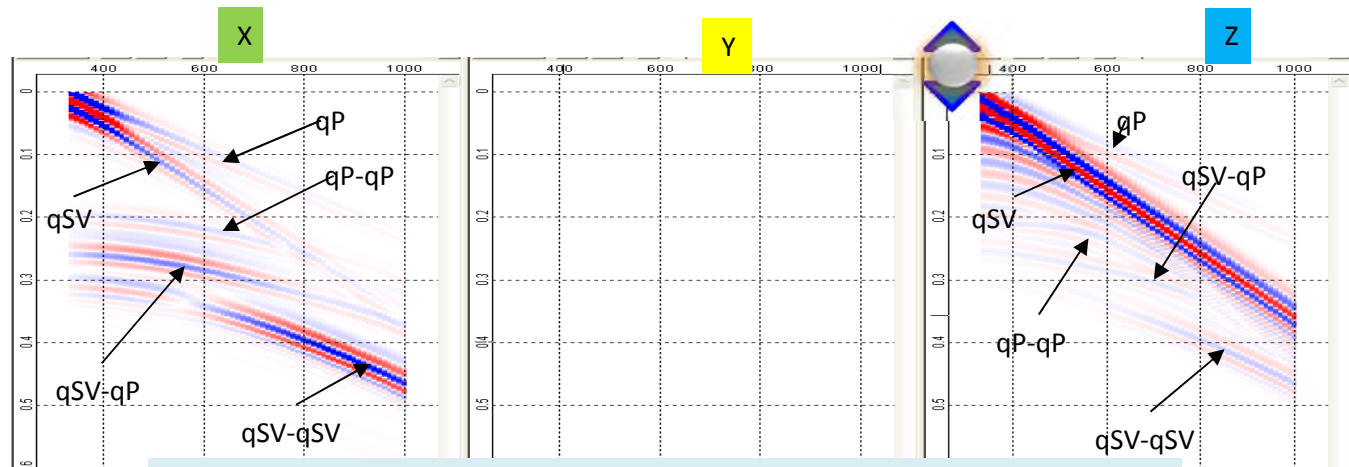
Since the modeling was carried out in an elastic medium, it is possible to also obtain the DWM image using converted waves.



Shotgathers of reflected waves for an excitation along OX axis



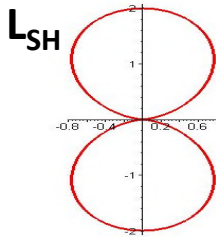
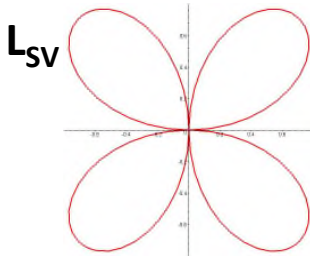
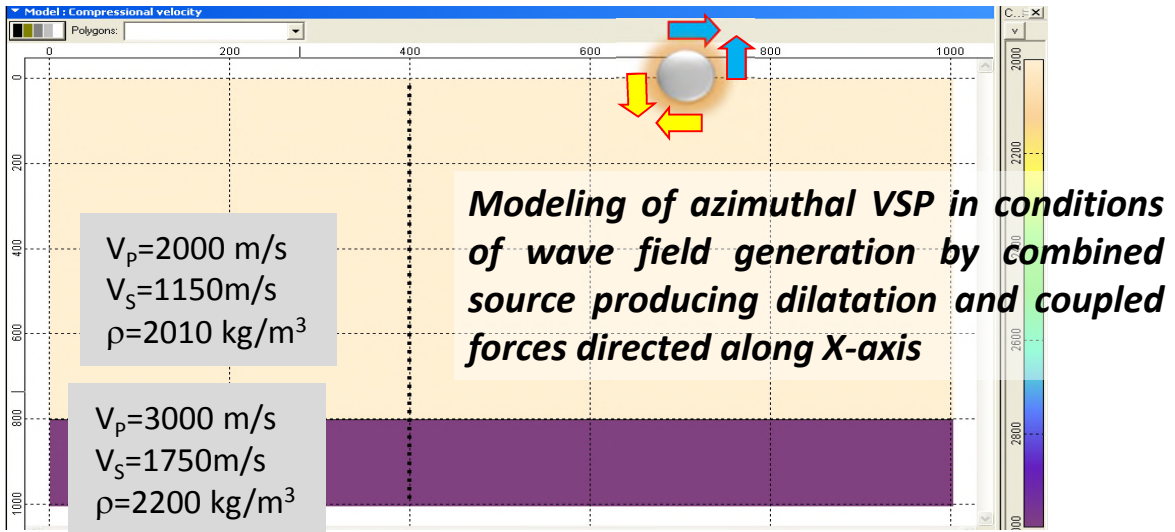
Shotgathers of reflected waves for an excitation along OY axis



Shotgathers of reflected waves for an excitation along OZ axis

Then, in those Slides, the 9C gathers are shown for source excitation along the X, Y, and Z axis, respectively.

It is interesting to compare the X component of 3C observation for source excitation along X axis and Y axis. The latter generates a pure SH wave. As contrary to the SV wave, the SH wave does not have wave-mode conversions in isotropic medium.



$$L_{SV} = \frac{\sin 2\theta \cos^2 \alpha}{8\pi\rho v_s^3}; \quad L_{SH} = \frac{\sin\theta \sin^2 \alpha}{4\pi\rho v_s^3}.$$

ϑ - angle of inclination of slowness vector in vertical plane

α - Azimuth of the slowness vector

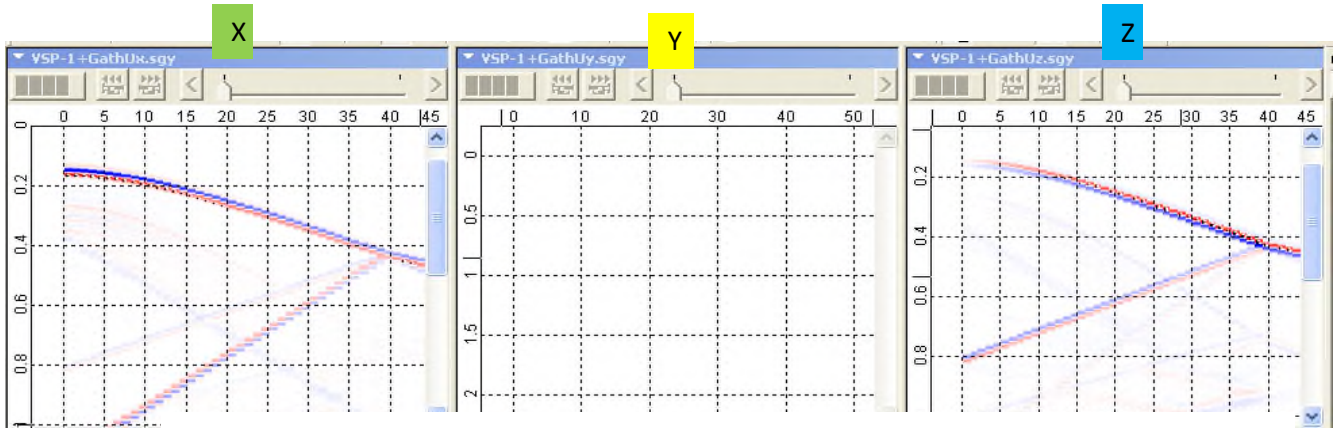
Characteristics of directional source of coupled forces

Since the monitoring observations for *hydrofrac* are often done inside wells. The next example is for the VSP with source located in different Y offset (crossline offset).

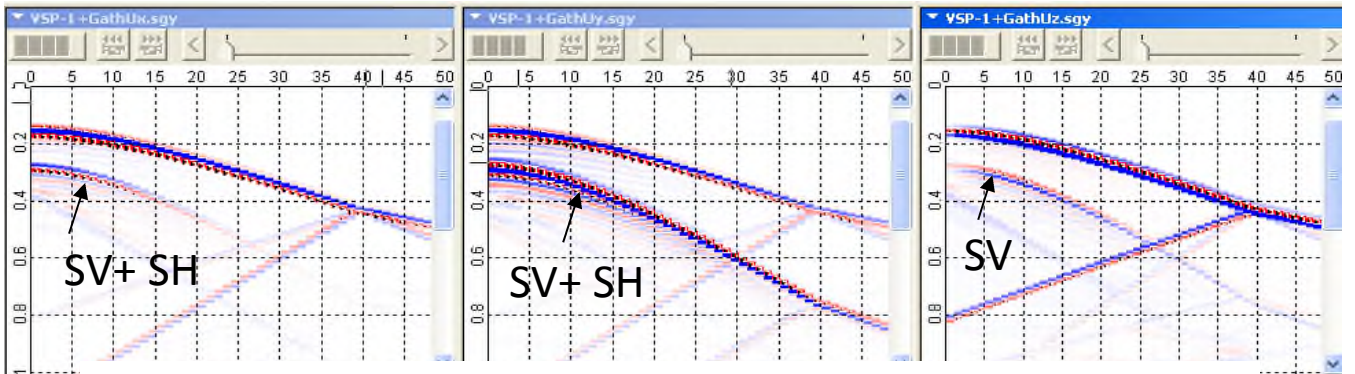
The model is shown in *this Slide*.

The S-wave azimuthal characteristics for the dipole source along the X axis are shown *below*.

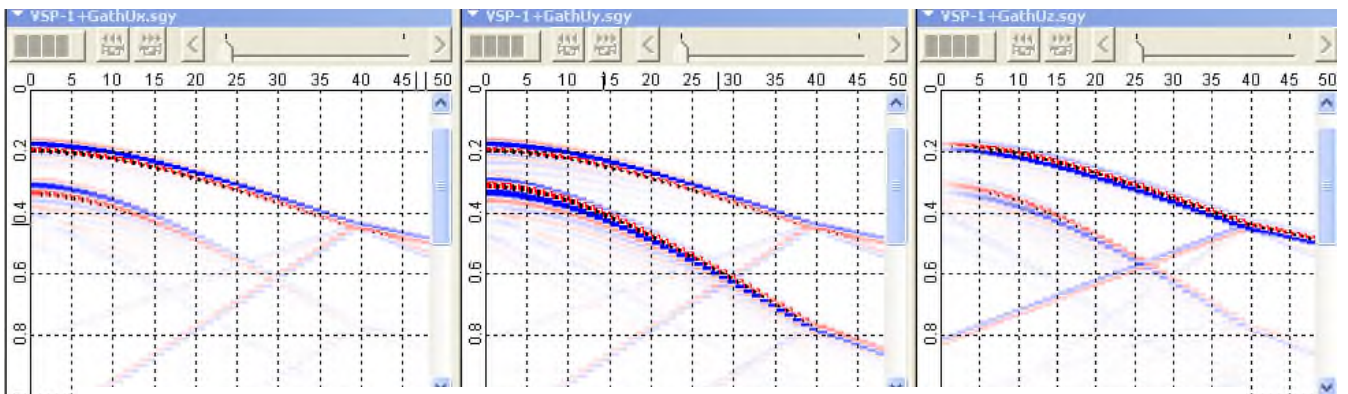
Three-component VSP synthetic shotgathers



Source position at X=700m, Y=0m; Well position at X=400m, Y=0m



Source position at X=700m, Y=100m; Well position at X=400m, Y=0m



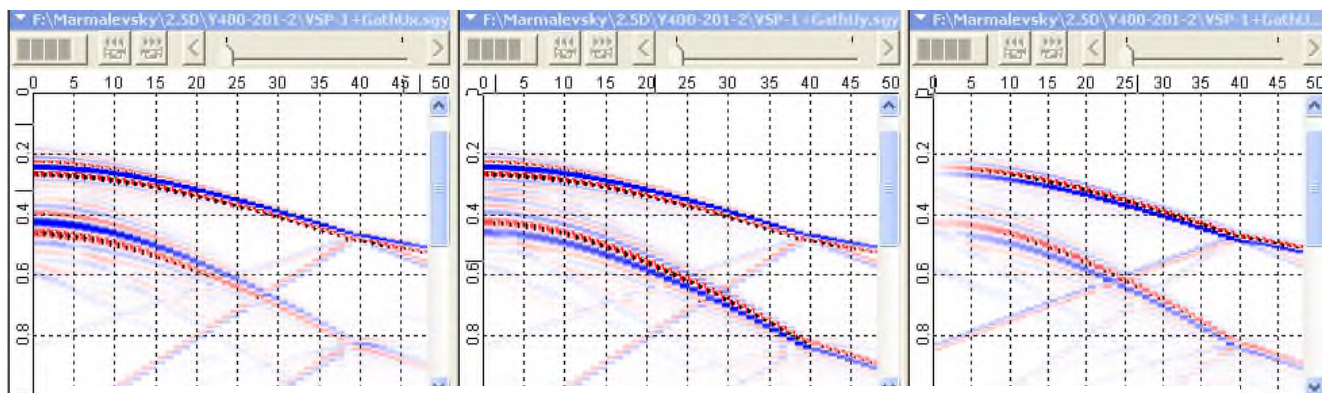
Source position at X=700m, Y=200m; Well position at X=400m, Y=0m

In this and next Slide, the gathers for a source with different Y offset are shown. All types of waves can be observed, in full conformity to the source-array characteristics.

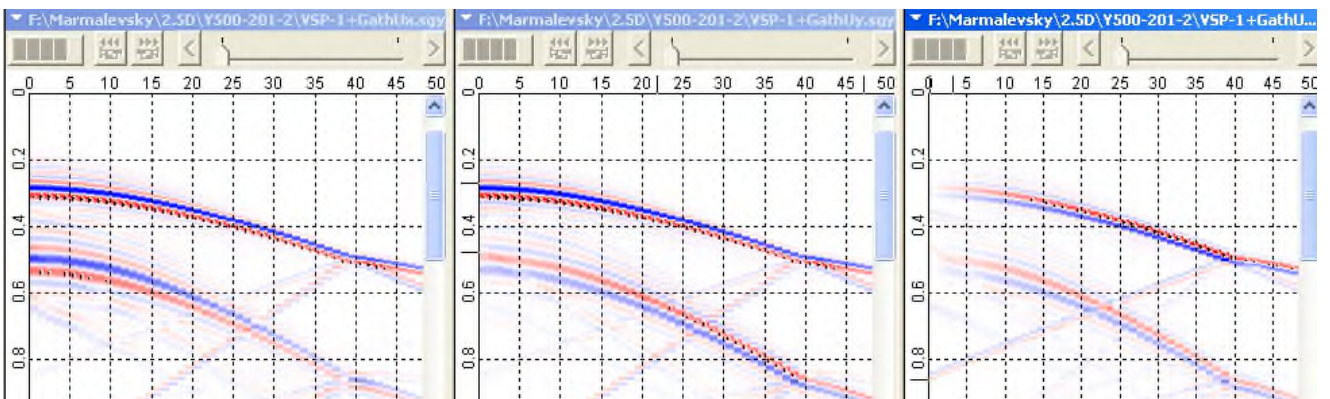
Three-component VSP synthetic shotgathers



Source position at X=700m, Y=300m; Well position at X=400m, Y=0m

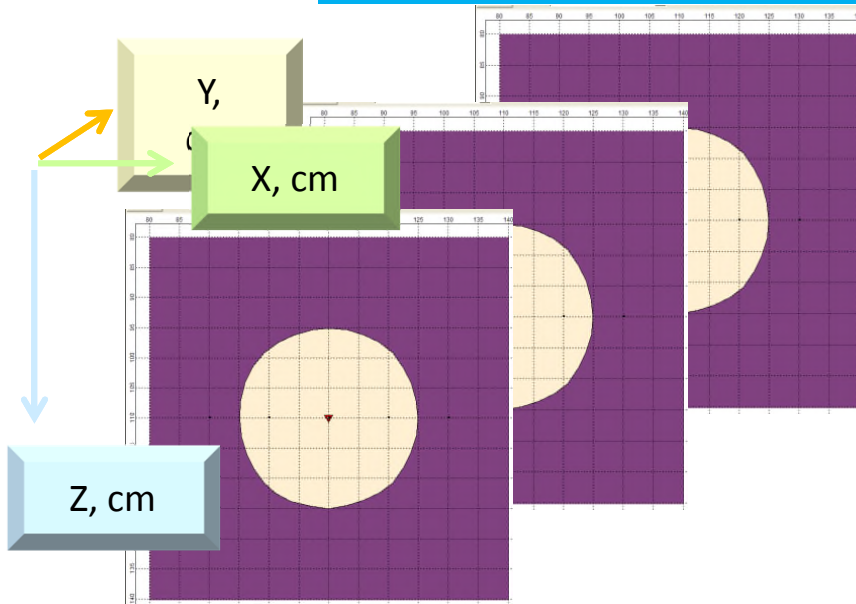


Source position at X=700m, Y=400m; Well position at X=400m, Y=0m



Source position at X=700m, Y=500m; Well position at X=400m, Y=0m

In this and previous Slide, the gathers for a source with different Y offset are shown. All types of waves can be observed, in full conformity to the source-array characteristics.



Model for simulating Lamb- Stoneley tube waves

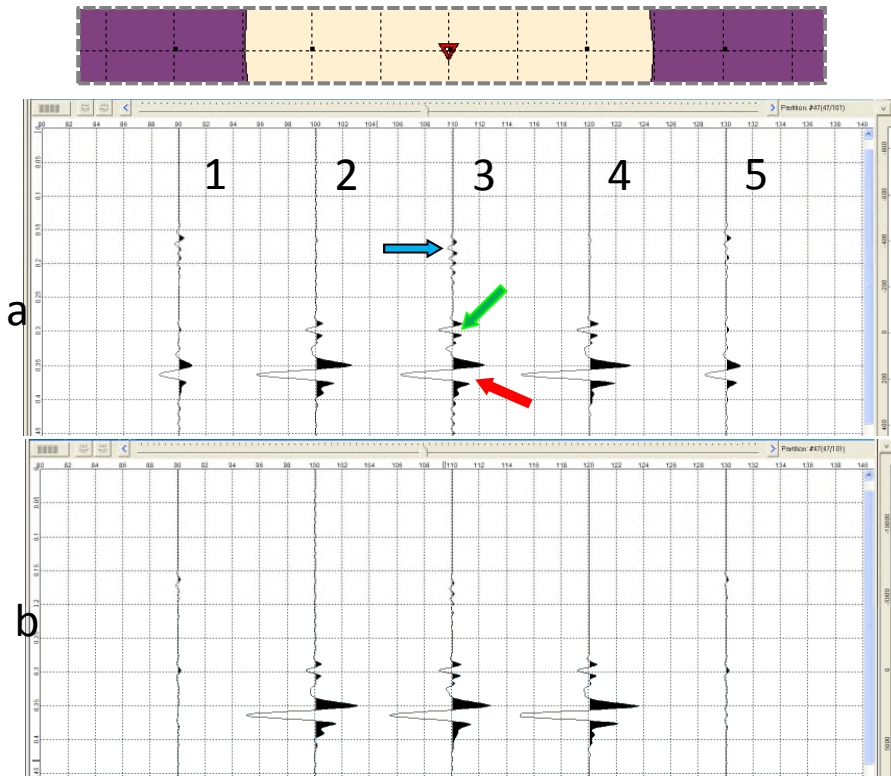
- Model of horizontally-oriented well in homogeneous surrounding medium
- Y-axis is perpendicular to the model image.
- Source peak frequency 50KHz
- Model is scaled to equivalent of 50Hz frequency of the source.
- *Well is filled with clay drilling mud (acoustic medium).*
- Borehole environment represents solid homogeneous medium (elastic) with higher velocity and density

The fact that the 2.5D modeling can simulate wave propagation in 3D space enable modeling the Lamb-Stoneley tube waves.

Theoretically, the velocity and the amplitude of the Lamb-Stoneley wave is depend only on the S-wave velocity inside the casing tube. In case that the well penetrates permeable fractured zone, S-wave velocity is changed, and the Lamb-Stoneley wave can be recorded in broadband acoustic logging.

In *this Slide* , the model of a well is shown, where the Y axis is chosen as the depth, i.e. this is the axis along which the medium parameters are constant locally. In this slide, the cross-section of the well's cylinder is shown, which is located in the X-Z plane. As contrary to the real situation, 5 receivers are deployed along the X axis at each recording depth (Z). Two of them are located outside the well.

The modeling parameters are selected proportionally to the acoustic logging frequencies and dimensions of the well.



Components :

a - Hydropohe (omnidirectional pressure);

b - Y- component of particle movement;

Receivers 1 and 5 are near the well walls in solid rock, 2, 3, 4 – inside well drilling mud.

Arrows:

blue – head wave, propagating in rocks,

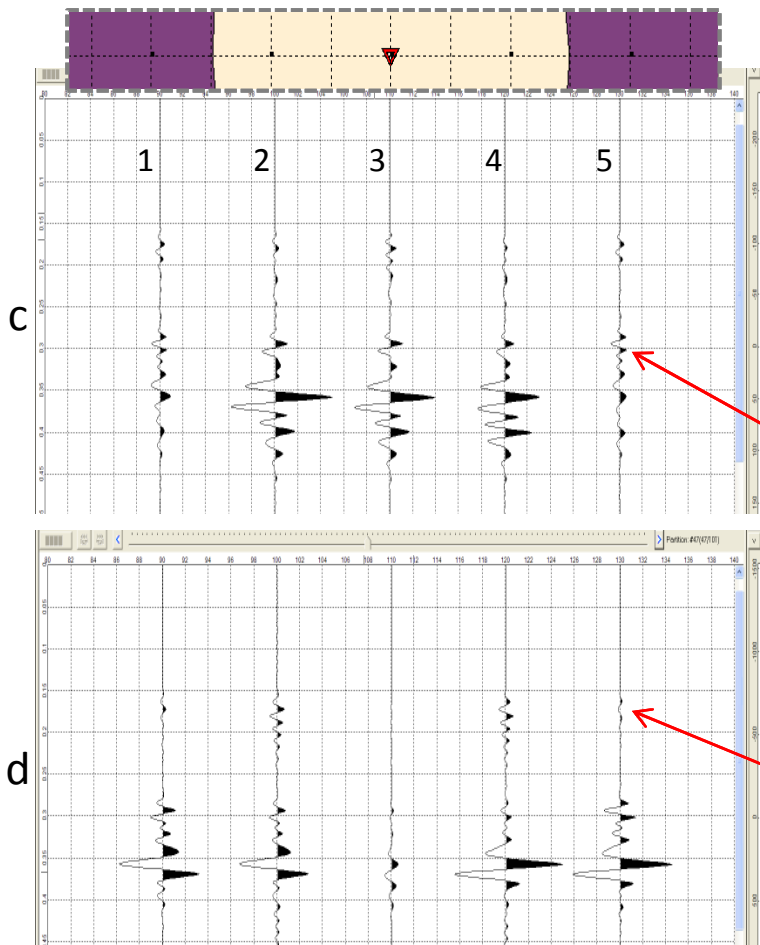
green – direct wave in water (55 Hz),

Red – tube wave (30 Hz)

It can be seen from this Slide that the Lamb-Stoneley wave is shear wave, and its velocity is lower than S-wave velocity in a liquid. Intensity of the Lamb-Stoneley wave in this case is higher, and its frequency is lower than the one of the direct waves propagating in the liquid.

It is also possible to observe that the Lamb-Stoneley wave is dramatically attenuated outside the well, and this reveals the well-known fact that it is hard to record such kind of waves by pressing down recording devices into the well's wall.

❖ Modeling of Lamb- Stoneley tube waves



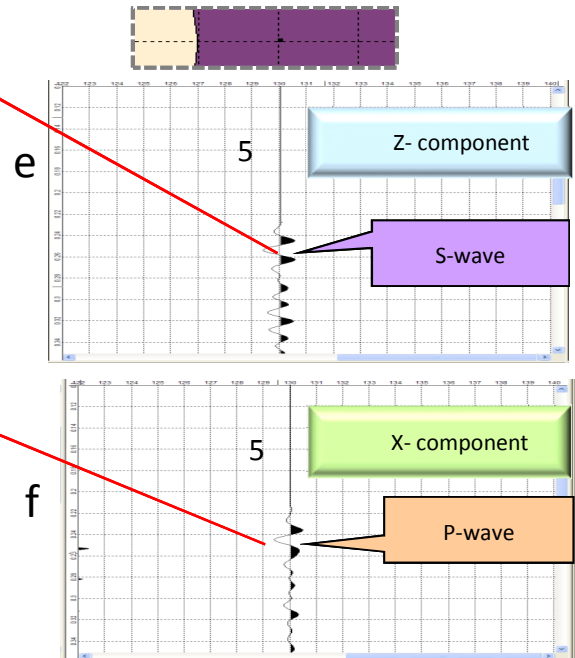
c - Z-component;

d - X-component;

Absolute amplitudes:

Y- component – **14 000**; X – 1 000; Z – 200;

Relatively big value of *Y-component* means than the wave is polarized along propagation direction, i.e. *is compression wave*.



For receiver near the well wall inside of solid rock

e - for Z-component – S-wave is recorded

f - for X-component – P-wave is recorded

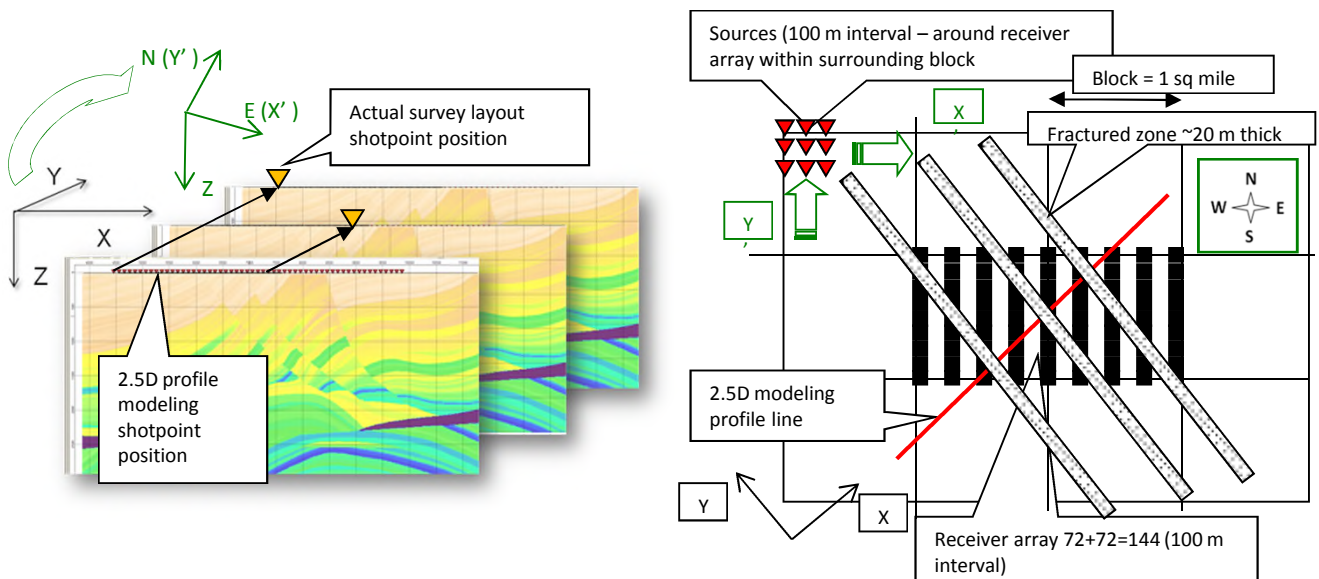
Arrival of P-wave is earlier(for 50Khz – 10 msec) than S-wave by 10 msec .

In *this Slide*, the example of the wave recorded by a pressure unit is shown. Here, the Z-component is shown in the top and the X component is shown at the bottom. Here the intensities of waves (absolute amplitude) for various components are also shown. The strongest signal at Y component is a P-wave arrival, because its sources and receivers are located close to the cylinder axis.

❖ Replicating the 2.5D-3C profile synthetic data

Orienting the profile for 2.5D-3C modeling directly along geological strike independently from 3D (3D-3C) seismic survey layout

- In case of considerable azimuth difference between geological strike and cross-lines of survey layout, more dense positioning of shotpoints and receivers are positioned along X- (2.5D profile orientation) and Y- (2.5D offsets) axis for 2.5D modeling application.
- Then, each of actual shotpoint and receiver locations on the 3D survey can be, in special way, mapped to the closest shotpoints and receivers positions in the 2.5D profile.
- By replicating the 2.5D profile synthetic data and doing linear coordinate transformation, together with some regular form of trace selection, we can achieve the required likeness to particular 3D (3D-3C) survey layout. This allows for bypassing 3D finite-difference modeling computations, which still are unproductively huge for elastic (elastic anisotropic) approximations of wave equation, and widening of this modeling technique application to industry scale modeling tasks in 3D (3D-3C) seismic prospecting and data interpretation.



This Slide shows the capability of 2.5D-3C modeling to generate synthetic 3C data for seismic survey layouts with orientation different from main geological strike (here, 2.5D model with Y-axis as the direction where model parameters are constant).

Summary

- Application of 2.5D-3C modeling for surface and VSP surveys allows designing the parameters of survey layouts from the viewpoint of their azimuth distribution, density of observation and resolution capability for solving different target tasks;
- 3D-9C modeling of seismic emission for vector source provides a tool for solving the very important problem of monitoring well fracking;
- 2.5D-3C modeling can be applied to modeling and interpretation of the Lamb-Stoneley tube waves used in wide-band sonic logging;
- Modeling of all types of waves for surface-based and well-based acquisition configurations may be done in a Linux cluster. The modeling for small 2.5D-3C models may be done on a single Window workstation;
- The total amount of computation can be reduced by tens, and sometimes - hundreds times, while maintaining all the features of 3D survey and following processing of 3D-3C (or conventional 3D-1C) seismic data.